concentration (10–20 %) of the CGF extract or of serum reduced this gene expression compared with the 0 % control (differentiation medium only) group (Fig. 2). Gene expression of runt-related transcription factor 2 (RUNX2) and of osterix (OSX), the key regulators of osteogenesis, were not significantly changed by treatment with the CGF extract (Fig. 2).

Effect of CGF extracts on proliferation of hTERT-E6/E7 cells

A previous study showed that a first-generation plasma concentrate (Ex.PRP) has a positive dose-dependent effect on cell proliferation [16]. However, other studies have reported the contradictory result that low concentrations of Ex.PRP (a few times greater than physiological levels) are more efficient at enhancing cell proliferation than very high concentrations [17–19]. In this study, the effect of a CGF extract on human mesenchymal stem cell proliferation was assessed by use of a cell count assay and hTERT-E6/E7 cells. In this study, the effect of a CGF extract or serum at concentrations of 1, 3, 5, 10, or 20 % in the culture medium was tested. hTERT-E6/E7 cell proliferation was promoted, in a dose-dependent fashion, by treatment with a CGF extract compared with the effect of serum addition. A significant difference between the effect of CGF and serum on cell proliferation was observed at all concentrations except 20 %. In particular, CGF extract at concentrations of 5 and 10 % markedly increased hTERT-E6/E7 proliferation (Fig. 3a).

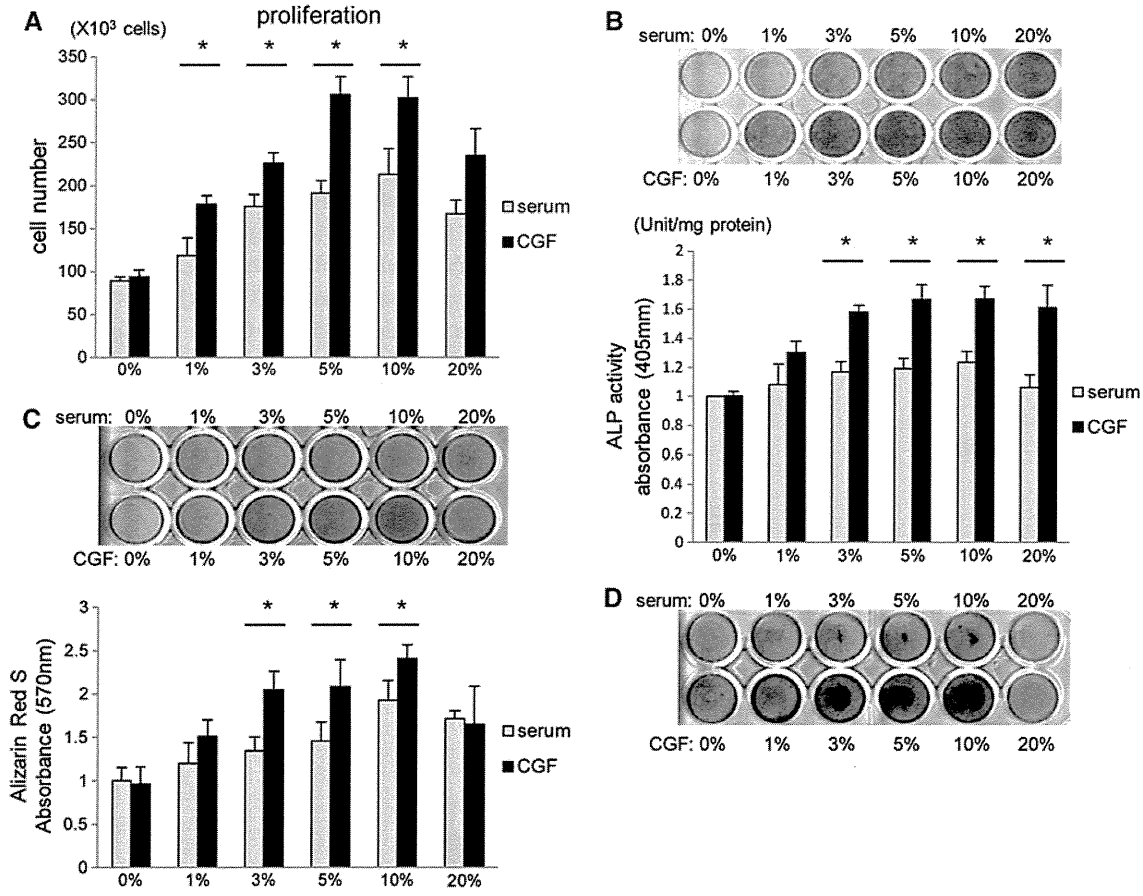

Fig. 3 Effect of a CGF extract on growth and osteoblastic differentiation of hTERT-E6/E7 mesenchymal cells. **a** Cell proliferation. hTERT-E6/E7 cells (5×10^3/well) were treated with different concentrations of a CGF extract or serum control for 24 h after which cell number was counted. **b** Alkaline phosphatase (ALP) staining and enzymatic activity. hTERT-E6/E7 cells were treated with different concentrations of a CGF extract or control serum for 4 days and were then subjected to ALP staining and activity assays. ALP activity was normalized to the protein content of each sample. **c**, **d** Mineralization. hTERT-E6/E7 cells were treated with different concentrations of a CGF extract or control serum for 21 days and were then stained with alizarin red S solution. The Ca content in the matrix of the cells was quantified by measuring the absorbance at 570 nm of the extract of the calcium bound dye. hTERT-E6/E7 cells were treated with different concentrations of a CGF extract or control serum for 21 days and were then stained with von Kossa solution. All data are mean ± SD from three independent experiments (each experiment used CGF from a different volunteer) performed in duplicate. (*$P < 0.05$ compared with the serum group of the same concentration.)

Effect of a CGF extract on the ALP staining and enzymatic activity of hTERT-E6/E7 cells

We next investigated the effect of a CGF extract on osteoblastic differentiation of hTERT-E6/E7 cells by ALP staining and ALP enzyme activity measurement after 4 days treatment with CGF or normal serum. CGF extract treatment increased ALP activity at all concentrations tested compared with the 0 % control (differentiation medium only) group. In addition when compared with equivalent serum dose groups, the CGF-induced increase in ALP activity was significantly different at CGF concentrations of 3–20 % (Fig. 3b).

Effect of CGF extract on mineralization of hTERT-E6/E7 cells

To further confirm the effect of CGF on osteoblastic differentiation, the effect of CGF on the mineralization of hTERT-E6/E7 cells was tested by alizarin red (Fig. 3c) and von Kossa staining (Fig. 3d). hTERT-E6/E7 cells were cultured with differentiation medium containing one of six different doses of a CGF extract or serum for 21 days. Alizarin red and von Kossa staining of these cells showed that CGF at concentrations between 3 and 10 % promoted calcification of the extracellular matrix (ECM) whereas calcification was not clearly observed in cells treated with CGF or serum at a concentration of 20 %. The extent of this ECM calcification was quantified by measurement of the absorbance of the alizarin red S solution. A CGF extract at a concentration between 3 and 10 % significantly increased calcification of the ECM compared with each equivalent concentration of serum.

Typical growth factors and inflammatory cytokines in CGF

We measured typical growth factors and inflammatory cytokines, including PDGF-BB, TGF-β1, TNF-α, and IL-1β, that were secreted by platelets. We found the CGF extract contained these cytokines at concentrations similar to or higher than those in serum. PRP contained high levels of inflammatory cytokines that might inhibit bone formation yet also contained high concentrations of cytokines that might promote bone formation. In a sustained-release test, we found CGF slowly released these cytokines for 9–13 days (Fig. 4).

Treatment of a rat calvaria critical-size bone defect with CGF and BMSCs: Micro-CT analysis

We next investigated the effect of CGF with or without BMSCs on bone regeneration using a representative critical-size bone defect model, the rat calvaria defect model. Representative 3D-reconstructed images of empty defect, CGF, and CGF + BMSC groups, assessed by micro-CT at

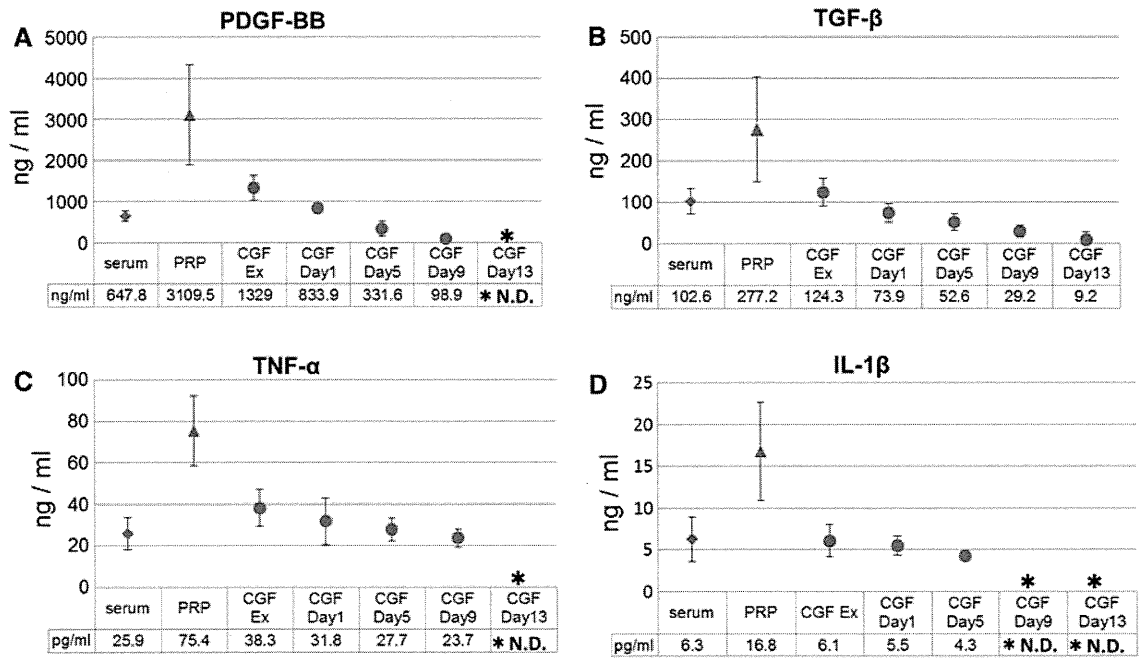

Fig. 4 Measurement of typical platelet cytokines. CGF, PRP, and serum were assayed for PDGF-BB, TGF-β1, TNF-α, and IL-1β by ELISA. In a sustained-release test we incubated CGF for 13 days at 37 °C in centrifuge tubes containing 1,000 μl PBS. The PBS in the tubes was replaced every 2 days and collected for ELISA. CGF slowly released these cytokines. **a** PDGF-BB, **b** TGF-β, **c** TNF-α, **d** IL-1β. *ND* not detected

4, 8, and 12 weeks, are shown in Fig. 5a. An increase in bone formation was observed for all groups over the 12-week period. However, the CGF group and the CGF + BMSC group seemed to regenerate bone better than the control (empty defect) group.

In the control group, bone regeneration was observed only at the periphery of the defect over the 12-week period. In the CGF group, new bone formation started at the peripheral area of the defect and then proceeded toward the center of the defect over time. However, in the CGF + BMSC group, new bone formation was observed not only at the periphery of the bone hole but also in the central area of the defect. This new, central bone included islands of new bone that had no contact with the cut edge of the host bone and that were observed starting from 4 weeks after operation. This group had almost completely repaired critical-size bone defects within 12 weeks after operation.

The total volume of mineralized bone within the defect sites was determined by analysis of the micro-CT images by use of Tri/3D Bon software. As shown in Fig. 5b, the volume of newly formed bone in the CGF + BMSC group was greater than that of the CGF group, and that of the CGF group was greater than that of the control group. Significant differences between the groups were found 4, 8, and 12 weeks after operation except for between the CGF and CGF + BMSC groups at 12 weeks ($n = 6$ for each group/period).

Treatment of a rat calvaria critical-size bone defect with CGF and BMSCs: histological findings

Histological assessment of the osteogenic potential of CGF and CGF + BMSC was performed 4, 8, and 12 weeks after operation in the above-described rat calvaria defect model.

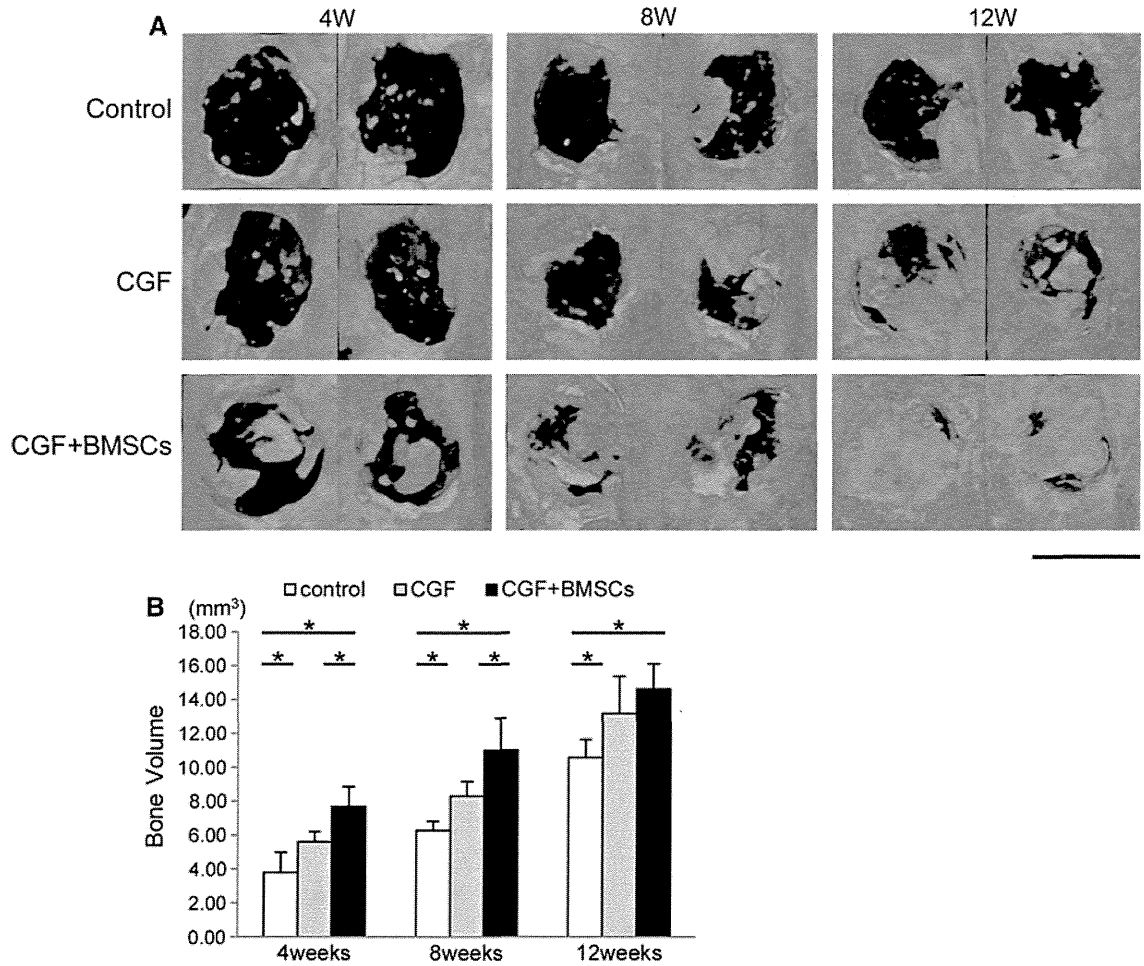

Fig. 5 Treatment of rat calvaria critical-size bone defects with CGF and BMSCs: micro-CT analysis. Bilateral, full thickness, critical-size bone defects (5.0 mm in diameter) were created in the parietal bones of Sprague–Dawley rats. These defects were treated by filling with CGF or CGF + bone marrow stromal cells (BMSCs), or were left unfilled as empty defect controls. **a** Representative microfocus computed tomography (micro-CT) images of cranial samples of the three groups 4, 8, and 12 weeks (W) after operation. *Bar* 5 mm. **b** Calculation of the volume of newly formed bone in calvaria defect sites in the three groups 4, 8, and 12 weeks after operation. All data are mean ± SD from six samples. (*$P < 0.05$)

Hematoxylin and eosin-stained (H&E) sections of bone were examined under a light microscope (Fig. 6a). In addition, we also analyzed 4-week samples by use of polarized light microscopy (Fig. 6b), because calcified immature bone tissue cannot be distinguished from collagenous fibrous tissue on decalcified H&E sections until several weeks after bone formation. Non-calcified woven bone is observed as shiny white fibrous tissue under a polarized light microscope [20, 21].

Histological analysis showed clear differences in tissue formation between the different treatment conditions. In the control group, sparse fibrous connective tissue was observed to traverse the empty defects and newly formed bone was only found in the area adjacent to the edges of the defect site 4 weeks after operation. Woven bone was not clearly observed in polarized microscopic images of the defect site. This pattern of bone formation was also observed after 8 and 12 weeks, except that the new bone at the periphery of the bone hole became thicker over time. Twelve weeks after operation, a large bone defect still remained in the control group.

In the CGF group, similar to the control group, only fibrous connective tissue was observed to traverse the defects and newly formed bone was observed at the edges of the defect site only 4 weeks after operation. However, in contrast with the control group, thin woven bone-like tissue was observed within the defects by polarized light microscopic analysis (Fig. 6b, white arrows). Over time, the new bone at the periphery gradually grew upwards to the central area of the defect site. Twelve weeks after operation, newly formed bone covered a large area of the bone defect.

In the CGF + BMSC group, islands of newly formed bone were observed 4 weeks after operation, which corresponded well with the micro-CT data obtained at this time. In contrast with the other two groups, newly formed bone was found both in the periphery and at the center of the defect site at this time. In addition, abundant neovascularization was observed around the new bone. The new bone became thicker over time, and, 12 weeks after the operation the critical-size bone defect was almost closed and bone marrow was confirmed to be present within the new bone tissues, resulting in a structure similar to that of normal cranial tissues.

Discussion

This study demonstrated that CGF, a second-generation platelet concentrate, effectively promoted the repair of bone defects and had particularly strong effects when combined with BMSCs. In a rat calvarial defect model, combined use of CGF and BMSCs almost completely repaired critical-size bone defects within 12 weeks. In addition, the CGF extract promoted the proliferation, osteogenic maturation, and mineralization of mesenchymal stem cells in vitro.

It is well established that in the rat calvarial defect model there is a gradual progression of new bone from the periphery of the bone hole to the center. New bone progresses in this direction because the cells that induce bone formation are mainly supplied from the cut edge of the bone defect. However, in our study, micro-CT and

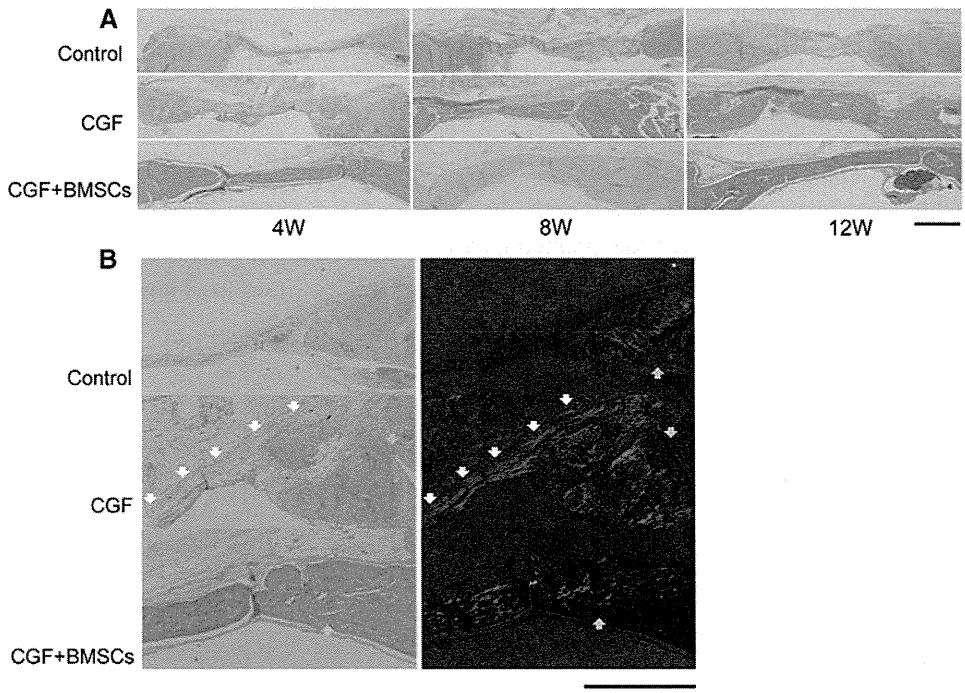

Fig. 6 Treatment of rat calvaria critical-size bone defects with CGF and BMSCs: histological findings. **a** Representative light microscopic images of cranial tissue sections of the three groups, stained with H&E 4, 8, and 12 weeks after operation. (magnification ×20). *Bar* 1,000 μm. **b** Representative light (*left column*) and polarized light (*right column*) microscopic images of H&E stained cranial tissue sections of the three groups 4 weeks after operation, focused on the edges of the cranial holes (magnification ×40). *Bar* 1,000 μm. The *yellow arrows* indicate the edges of the cranial holes. The *white arrows* indicate woven bone tissue (shiny white fibrous tissue)

histological examination revealed new bone formation not only at the periphery of the bone hole but also in the central area of the bone defect in the CGF + BMSCs group, starting 4 weeks after the operation. This new bone included island-shaped new bone that had no contact with the cut edge of the periphery of the bone. Twelve weeks after the operation, critical-size bone defects were almost closed over in the CGF + BMSCs group, whereas large bone defects remained in the control group. This finding suggested that the fibrin network of CGF served as a scaffold for BMSCs that supported the formation of new bone by BMSCs, as reported by Dohan, Choukroun et al. [2, 22, 23]. In addition, new bone mass significantly increased in the CGF and CGF + BMSCs groups starting 4 weeks after operation, compared with the control group, and this tendency continued until 12 weeks after operation.

Although very favorable results were obtained in these in-vivo experiments, the in-vitro effects of the CGF extract were different depending on the concentration of CGF used. The in-vitro experiments suggested that a highly concentrated CGF extract may inhibit osteogenic maturation and mineralization. Thus, whereas CGF extracts at concentrations between 1 and 10 % promoted cellular proliferation, osteogenic maturation, and mineralization in a dose-dependent manner, the effects of a 20 % CGF extract were inferior to those of the 10 % group, suggesting the existence of optimum doses of CGF. With regard to its effect on *COL1A1* gene expression, expression of this gene decreased in the presence of a high concentration (20 %) of CGF compared with its expression in the control group (0 %), indicating that CGF might actually function to inhibit bone formation. We speculate that this inhibitory effect of CGF might be because, as reported by Dohan et al. [4], the CGF extract contains not only growth factors favorable for bone formation but also inflammatory cytokines, for example tumor necrosis factor-α (TNF-α) and interleukin-1 (IL-1), which may inhibit bone formation (Fig. 4). Therefore, at a high concentration of CGF the inhibitory action of inflammatory cytokines on bone formation may dominate over the promoting action of the growth factors, which would result in unfavorable effects on bone formation. This concentration-dependent effect seems to be one of the reasons why contradictory effects of PRP on bone formation have been described in previous reports [8–10]. In addition, the results from polymerase chain reaction (PCR) analysis in this study did not reveal any significant change in the expression of such osteogenic master genes as RUNX2 and OSX, which determine whether MSCs are directed toward differentiation into osteoblasts, irrespective of the concentration of CGF extract. These results suggest that the CGF extract stimulates osteogenic maturation only and does not promote commitment of MSCs to osteoblast differentiation.

In this study, we found that CGF served as a good scaffold for BMSCs for treatment of a critical-size bone defect model. The advantages of using CGF as a scaffold are:

1. CGF contains cytokines that promote cell growth, maturation, and matrix production;
2. CGF preparation and cell integration into CGF, are quick and easy; and
3. CGF is safe because it contains nothing but autologous blood ingredients.

For all these reasons we assume CGF will also work as a good scaffold for bone regeneration when it is applied clinically. However, when considering the actual clinical application of combination therapy of CGF and cell transplantation, it will be necessary to optimize the cells to be used (their origin and preparation) and the amount of CGF and other ingredients or modifications that must be applied.

Conclusion

CGF promoted the proliferation, osteogenic maturation, and mineralization of mesenchymal stem cells in vitro, and combination therapy of CGF with BMSCs enabled excellent healing of a critical-size bone defect in vivo. CGF in combination with mesenchymal cell transplantation may be suitable for treatment of large bone defects that are difficult to treat by other methods. However, further research and optimization of the cells and CGF used, and other conditions, are needed before clinical application.

Acknowledgments We thank Dr Junya Toguchida, Kyoto University, for kindly providing the hTERT-E6/E7 cells and Mrs Mari Shinkawa for technical assistance with the histological study. This study was supported by a Grant-in-Aid for Scientific Research (no. 23390364) from the Ministry of Education, Culture, Sports, Science, and Technology, Japan, and by a special research subsidy from Terumo Life Science Foundation. The funders had no role in study design, data collection and analysis, decision to publish, or preparation of the manuscript.

Conflict of interest No competing financial interests exist.

References

1. Mosesson MW, Siebenlist KR, Meh DA. The structure and biological features of fibrinogen and fibrin. Ann N Y Acad Sci. 2001;936:11–30.
2. Dohan DM, Choukroun J, Diss A, Dohan SL, Dohan AJ, Mouhyi J, et al. Platelet-rich fibrin (PRF): a second-generation platelet concentrate. Part I: technological concepts and evolution. Oral Surg Oral Med Oral Pathol Oral Radiol Endod. 2006;101:e37–44.
3. Dohan DM, Choukroun J, Diss A, Dohan SL, Dohan AJ, Mouhyi J, et al. Platelet-rich fibrin (PRF): a second-generation platelet

concentrate. Part II: platelet-related biologic features. Oral Surg Oral Med Oral Pathol Oral Radiol Endod. 2006;101:e45–50.
4. Dohan DM, Choukroun J, Diss A, Dohan SL, Dohan AJ, Mouhyi J, et al. Platelet-rich fibrin (PRF): a second-generation platelet concentrate. Part III: leucocyte activation: a new feature for platelet concentrates? Oral Surg Oral Med Oral Pathol Oral Radiol Endod. 2006;101:e51–5.
5. Brown LF, Lanir N, McDonagh J, Tognazzi K, Dvorak AM, Dvorak HF. Fibroblast migration in fibrin gel matrices. Am J Pathol. 1993;142:273–83.
6. Marx RE, Carlson ER, Eichstaedt RM, Schimmele SR, Strauss JE, Georgeff KR. Platelet-rich plasma: growth factor enhancement for bone grafts. Oral Surg Oral Med Oral Pathol Oral Radiol Endod. 1998;85:638–46.
7. Pietrzak WS, Eppley BL. Platelet rich plasma: biology and new technology. J Craniofacial Surg. 2005;16:1043–54.
8. Plachokova AS, Nikolidakis D, Mulder J, Jansen JA, Creugers NH. Effect of platelet-rich plasma on bone regeneration in dentistry: a systematic review. Clin Oral Implant Res. 2008;19:539–45.
9. Freymiller EG, Aghaloo TL. Platelet-rich plasma: ready or not? J Oral Maxillofac Surg Off J Am Assoc Oral Maxillofac Surg. 2004;62:484–8.
10. Schmitz JP, Hollinger JO. The biology of platelet-rich plasma. J Oral Maxillofac Surg Off J Am Assoc Oral Maxillofac Surg. 2001;59:1119–21.
11. Dohan Ehrenfest DM, Rasmusson L, Albrektsson T. Classification of platelet concentrates: from pure platelet-rich plasma (P-PRP) to leucocyte- and platelet-rich fibrin (L-PRF). Trends Biotechnol. 2009;27:158–67.
12. Sohn DS, Heo JU, Kwak DH, Kim DE, Kim JM, Moon JW, et al. Bone regeneration in the maxillary sinus using an autologous fibrin-rich block with concentrated growth factors alone. Implant Dent. 2011;20:389–95.
13. Dohan Ehrenfest DM, de Peppo GM, Doglioli P, Sammartino G. Slow release of growth factors and thrombospondin-1 in Choukroun's platelet-rich fibrin (PRF): a gold standard to achieve for all surgical platelet concentrates technologies. Growth Factors (Chur, Switzerland). 2009;27:63–9.
14. He L, Lin Y, Hu X, Zhang Y, Wu H. A comparative study of platelet-rich fibrin (PRF) and platelet-rich plasma (PRP) on the effect of proliferation and differentiation of rat osteoblasts in vitro. Oral Surg Oral Med Oral Pathol Oral Radiol Endod. 2009;108:707–13.
15. Okamoto T, Aoyama T, Nakayama T, Nakamata T, Hosaka T, Nishijo K, et al. Clonal heterogeneity in differentiation potential of immortalized human mesenchymal stem cells. Biochem Biophys Res Commun. 2002;295:354–61.
16. Lucarelli E, Beccheroni A, Donati D, Sangiorgi L, Cenacchi A, Del Vento AM, et al. Platelet-derived growth factors enhance proliferation of human stromal stem cells. Biomaterials. 2003;24:3095–100.
17. Graziani F, Ivanovski S, Cei S, Ducci F, Tonetti M, Gabriele M. The in vitro effect of different PRP concentrations on osteoblasts and fibroblasts. Clin Oral Implant Res. 2006;17:212–9.
18. Weibrich G, Hansen T, Kleis W, Buch R, Hitzler WE. Effect of platelet concentration in platelet-rich plasma on peri-implant bone regeneration. Bone. 2004;34:665–71.
19. Choi BH, Zhu SJ, Kim BY, Huh JY, Lee SH, Jung JH. Effect of platelet-rich plasma (PRP) concentration on the viability and proliferation of alveolar bone cells: an in vitro study. Int J Oral Maxillofac Surg. 2005;34:420–4.
20. Sverzut CE, Lucas MA, Sverzut AT, Trivellato AE, Beloti MM, Rosa AL, et al. Bone repair in mandibular body osteotomy after using 2.0 miniplate system—histological and histometric analysis in dogs. Int J Exp Pathol. 2008;89:91–7.
21. Retamoso LB, Montagner F, Camargo ES, Vitral RW, Tanaka OM. Polarized light microscopic analysis of bone formation after inhibition of cyclooxygenase 1 and 2. Anat Record 2010;293:195–9.
22. Choukroun J, Diss A, Simonpieri A, Girard MO, Schoeffler C, Dohan SL, et al. Platelet-rich fibrin (PRF): a second-generation platelet concentrate. Part IV: clinical effects on tissue healing. Oral Surg Oral Med Oral Pathol Oral Radiol Endod. 2006;101:e56–60.
23. Choukroun J, Diss A, Simonpieri A, Girard MO, Schoeffler C, Dohan SL, et al. Platelet-rich fibrin (PRF): a second-generation platelet concentrate. Part V: histologic evaluations of PRF effects on bone allograft maturation in sinus lift. Oral Surg Oral Med Oral Pathol Oral Radiol Endod. 2006;101:299–303.

Biomaterials 34 (2013) 2185–2193

Contents lists available at SciVerse ScienceDirect

Biomaterials

journal homepage: www.elsevier.com/locate/biomaterials

Repair of meniscal lesions using a scaffold-free tissue-engineered construct derived from allogenic synovial MSCs in a miniature swine model

Yu Moriguchi [a], Kosuke Tateishi [a], Wataru Ando [a], Kazunori Shimomura [a], Yasukazu Yonetani [a], Yoshinari Tanaka [b], Keisuke Kita [b], David A. Hart [c], Alberto Gobbi [d], Konsei Shino [a], Hideki Yoshikawa [a], Norimasa Nakamura [a,e,f,*]

[a] Department of Orthopaedics, Osaka University Graduate School of Medicine, Osaka, Japan
[b] Department of Orthopaedic Sports Medicine, Osaka Rosai Hospital, Sakai, Japan
[c] McCaig Institute for Bone & Joint Health, University of Calgary, Calgary, Canada
[d] Orthopaedic Arthroscopic Surgery International, Milan, Italy
[e] Institute for Medical Science in Sports, Osaka Health Science University, Osaka, Japan
[f] The Center for Advanced Medical Engineering and Informatics, Osaka University, Osaka, Japan

ARTICLE INFO

Article history:
Received 31 October 2012
Accepted 22 November 2012
Available online 20 December 2012

Keywords:
Meniscal repair
Tissue engineering
Allogeneic
Stem cell
Synovium

ABSTRACT

The menisci of the knee are fibro-cartilaginous tissues and play important roles in the joint, and the loss of the meniscus predisposes the knee to degenerative changes. However, the menisci have limited healing potential due to the paucity of vascularity. The purpose of the present study was to test the feasibility of a scaffold-free tissue-engineered construct (TEC) derived from synovial mesenchymal stem cells (MSCs) to repair incurable meniscal lesions. Porcine synovial MSCs were cultured in monolayers at high density in the presence of ascorbic acid followed by the suspension culture to develop a three-dimensional cell/matrix construct (TEC). A 4-mm cylindrical defect was created bilaterally in the medial meniscus of skeletally mature miniature pigs. The defects were implanted with an allogenic TEC or were left empty. After 6 months, the TEC-treated defects were consistently repaired by a fibro-cartilaginous tissue with good tissue integration to the adjacent host meniscal tissue, while the untreated were either partially or not repaired. The ratio of Safranin O positive area within the central body of the meniscus adjacent to the original defect was significantly higher in the TEC-treated group than in the control group. Moreover, TEC treatment significantly reduced the size and severity of post-traumatic chondral lesions on the tibial plateau. These results suggest that the TEC could be a promising stem cell-based implant to repair meniscal lesions with preventive effects from meniscal body degeneration and the development of post-traumatic arthritis.

1. Introductions

The menisci of the knee are fibro-cartilaginous tissues with a unique matrix structure [1]. These tissues play important roles in controlling knee stability [2,3], shock absorption [2], and load distribution [4,5]. The menisci are not entirely vascularized, and a blood supply is found only in the outer third of its structure [6,7]. When a lesion/defect involves the avascular portion of the tissue, an effective biological repair cannot be expected even after stabilization since the repair process emanates to a significant degree from vascular damage. Currently, damage to the inner avascular zone of the meniscus is usually treated by resection via arthroscopic partial meniscectomy, which alleviates symptoms. However, studies on the biomechanics of the knee joint have demonstrated that articular contact pressure is significantly increased following even a partial meniscectomy [8,9]. In knees after removal of menisci, the articular contact area is reduced by approximately 50% [4], and the shock-absorbing capacity is reduced by approximately 20% in comparison with normal knees [10]. Such altered biomechanics of the knee joint following meniscectomy could affect the cartilage composition and metabolism, and result in alterations in the collagen fiber component of the superficial layer of the articular cartilage [11]. Indeed, several studies in animal models including rabbit [12–15], dog [16,17], sheep [18], and monkey [19], as well as clinical studies [20–22] have demonstrated the direct relationships between partial or total meniscectomy and the development of osteoarthritis.

* Corresponding author. Institute for Medical Science in Sports, Osaka Health Science University, 1-9-27 Tenma, Osaka City, Osaka 530-0043, Japan. Tel.: +81 6 6352 0093; fax: +81 6 6352 5995.
E-mail addresses: norimasa.nakamura@ohsu.ac.jp, n-nakamura@ort.med.osaka-u.ac.jp (N. Nakamura).

0142-9612/$ – see front matter © 2012 Elsevier Ltd. All rights reserved.
http://dx.doi.org/10.1016/j.biomaterials.2012.11.039

Accordingly, there is a need to save the damaged meniscus with the restoration of the structure and function.

Recent studies have shown the potential application of cell-based approaches for the repair of meniscal defects not effectively influenced by endogenous repair mechanisms. Some have demonstrated the efficacy of meniscal cells or chondrocyte-based approaches [23], however, other studies suggest limitations in these approaches as the reparative capacity of these cells may significantly decline with aging and culture passage [24,25]. In this regard, use of mesenchymal stem cells (MSCs) could be a potential alternative based on maintenance of their proliferative and differentiation capacity [26] regardless of aging [27,28], and it has been revealed that MSCs are present in various tissues [29,30]. Among them, we have focused on MSCs derived from synovium. A canine study on meniscal healing demonstrated the infiltration of blood vessels from synovium to the meniscal defect to facilitate repair [31], suggesting the involvement of synovial cells in meniscal repair. Moreover, synovium can be obtained by minimally invasive procedure such as arthroscopic surgery and has an ability to heal sufficiently after surgical excision, indicating the relative ease to obtain the tissue with minimal donor-site morbidity. Taken together, it may be a reasonable approach to use synovial MSCs to facilitate repair of otherwise non-repairing meniscal lesions. On the other hand, although recent small animal studies on synovial MSC-based therapy in meniscus used the direct injection procedure approach [32,33], it is also reasonable to consider the use of scaffolds, specifically in clinically relevant large animal studies, which in theory can provide mechanical stability to the injured site while allowing for cell attachment and proliferation under a protected three-dimensional environment [34]. However, a number of concerns still remain associated with the use of such animal or chemical polymer-derived materials contained in scaffolds in terms of the long-term efficacy and safety [35–38]. In order to avoid such unknown risks followed by implantation surgery, such materials should ideally be excluded throughout the treatment procedure.

To address such concerns, we have developed a scaffold-free tissue-engineered construct (TEC) derived from synovial mesenchymal stem cells [39]. The TEC contains undifferentiated MSCs at high density in a three-dimensional matrix which has been synthesized by the MSCs themselves. Although scaffold-free, the TEC possesses sufficiently self-supporting mechanical properties to withstand surgical handling and exhibits an effective tissue-adherent capacity with abundant expression of adhesion molecules such as fibronectin [28,39,40]. Moreover, TEC have the capacity to differentiate into hyaline cartilaginous tissues *in vitro*, and allogenic TEC promoted cartilage repair in a porcine injury model [28,39].

Based on such biological and material properties, such TEC likely also has good potential to repair injured menisci, a fibro-cartilaginous tissue in the knee joint. The purpose of this study was to test the feasibility of the allogenic TEC approach to develop fibro-cartilaginous tissue *in vitro* and to repair otherwise inadequately repairing meniscal lesions in a large animal, the mature minipig model.

2. Materials and methods

All procedures of this study followed the Declaration of Helsinki principles. The committee on the Ethics of Animal Experiments in Osaka University approved all animal procedures.

2.1. Harvest of synovial tissue and isolation of the cells

Porcine synovial membranes were obtained aseptically from the knee joints of skeletally mature miniature male pigs (12 months of age) ($n = 4$) within 12 h of death. The cell isolation protocol was essentially that used previously for the isolation of human synovial-derived MSCs [40]. Briefly, synovial membrane specimens were rinsed with phosphate-buffered saline (PBS), minced meticulously, and digested with 0.4% collagenase (Worthington Biochemical, Lakewood, NJ) in high-glucose Dulbecco's modified Eagle's medium (HG-DMEM; Gibco BRL, Life Technologies, Rockville, MD) for 2 h at 37°C. After neutralization of the collagenase by growth medium containing DMEM supplemented with 10% fetal bovine serum (FBS; HyClone, Logan, UT) and 1% Penicillin–Streptomycin (Gibco BRL, Life Technologies), the cells were collected by centrifugation, washed with PBS, resuspended in the growth medium, and plated in culture dishes. These cells were defined as MSCs [29,30,39]. For subsequent expansion, MSCs were cultured in the growth medium at 37°C in a humidified atmosphere of 5% CO_2, with the medium replaced once per week. After 15–28 days of primary culture, when the cells reached confluence, cells were washed twice with PBS, harvested by treatment with trypsin–EDTA (0.25% trypsin and 1 mM EDTA; Gibco BRL, Life Technologies), and replated at 1:3 dilution for the first subculture. Cell passages were continued in the same manner with 1:3 dilution when cells reached confluence. Cells at passages 4–7 were used in the present studies.

2.2. Development of the TEC

Synovial MSCs were plated on culture dishes at a density of 4.0×10^5 cells/cm^2 in the growth medium containing 0.2 mM ascorbate-2-phosphate (Asc-2P), an optimal concentration from earlier studies [39]. Within a day, the cells became confluent. After an additional 7–14 days in culture, a complex of the cultured cells and the ECM synthesized by the cells was detached from the substratum by application of shear stress using gentle pipetting. The detached monolayer complex was left in suspension to form a three-dimensional structure by active tissue contraction. This tissue was termed a basic scaffold-free three-dimensional TEC [39].

2.3. In vitro fibro-chondrogenesis

Approximately 2×10^5 cells were placed in a 15-ml polypropylene tube (BD Falcon), and centrifuged at 500 g for 10 min. The pellet was cultured at 37°C with 5% CO_2 in 500 μl of chondrogenic culture medium that contained HG-DMEM with 0 (serum free), 2, or 10% FBS, supplemented with 50 μg/ml ascorbate-2-phospate, 100 μg/ml sodium pyruvate, and 50 mg/ml ITS+ Premix (BD Biosciences; 6.25 μg/ml insulin, 6.25 μg/ml transferrin, 6.25 ng/ml selenious acid, 1.25 mg/ml BSA, and 5.35 mg/ml linoleic acid), and 200 ng/ml recombinant human BMP2 (a gift from Osteopharma Inc., Osaka, JP). The medium was replaced twice per week for 3 weeks. In the control group, the pellet was cultured in the growth medium (HG-DMEM with 10% FBS). The optimal concentration of rhBMP2 was determined from preliminary *in vitro* optimization studies on chondrogenic differentiation of MSCs in pellet [39,40].

2.4. Histological assessment of the cell pellets

The cell pellet cultures were fixed in 4% paraformaldehyde, rinsed twice with PBS, embedded in paraffin, cut into 4 μm sections, and then stained for 2 h at room temperature with 1% Alcian blue (Alcian Blue 8GX; Sigma, Missouri, USA) in 0.1 N HCl, and subsequently counter stained with Kernechtrot.

2.5. Quantitative reverse transcription-polymerase chain reaction (qRT-PCR)

Quantitative RT-PCR was used to determine the expression of cartilage-specific genes (collagen II and aggrecan), a chondrocyte dedifferentiation marker (collagen I) and a housekeeping gene (GAPDH). For RNA extraction, pellets were homogenized in Buffer RLT for approximately 60 s. Lysate was then centrifuged, and supernatant was removed. Total RNA was extracted using an RNeasy Fibrous Tissue Kit (Qiagen, Valencia, CA, USA). After measuring RNA concentration for each sample, complementary DNAs (cDNAs) were obtained by RT of 1 μg total RNA using a Reverse Transcription System (Promega, San Luis Obispo, CA, USA) with random primers. Samples were prepared for qRT-PCR using SYBR® Premix Ex Taq (TaKaRa, JP) and custom designed porcine primers. qRT-PCR was then performed on an ABI PRISM 7900HT (Applied Biosystems, Foster City, CA 94404, USA). Pellets cultured in HG-DMEM with 10% FBS without any chondrogenic supplements were served as a reference (calibrator) for the comparison of mRNA levels for the differentiated pellets (0, 2, or 10% FBS). Gene expression was normalized to the level of GAPDH using the formula $2 - \Delta CT$, where CT is the threshold cycle and $\Delta CT = CT$ (target gene) − CT (GAPDH). For each gene, the normalized mRNA level in each sample was calculated relative to that in the calibrator using the formula $2 - \Delta\Delta CT$, where $\Delta\Delta CT = \Delta CT$ (sample) − ΔCT (calibrator). Primers were designed with Primer 3 software based on the GenBank database sequences corresponding to the specific gene Accession Number. PCR primers used were as follows: pig-GAPDH (forward): CTG CCC CTT CTG CTG ATG C, (reverse): CAT CAC GCC ACAGTT TCC CA, pig-aggrecan (forward): ATT GTAGGACCC AAAGGACCT C, (reverse): GGT CCC AGG TTC TCC ATC TC, pig-collagen 1a2 (forward): ATT GTAGGACCC AAAGGACCT C, (reverse): GGT CCC AGG TTC TCC ATC TC, pig-collagen 2a1 (forward): ATT GTAGGACCC AAAGGACCT C, (reverse): GGT CCC AGG TTC TCC ATC TC.

2.6. Implantation of in vitro generated TEC into medial meniscus defects

Skeletally mature female miniature pigs ($n = 6$) were anesthetized by intramuscular injection of a mixture of ketamine hydrochloride (50 mg/ml and 0.6 ml/kg of body weight) and xylazine (20 mg/ml and 0.3 ml/kg of body weight), and continuous

intravenous injection of propofol (10 mg/ml and 8 ml/kg/h). Bilateral longitudinal paramedian incisions were made in the medial aspect of the pig knees. The vastus medialis muscle was largely preserved and dissected for 2 cm in its distal fibers. The capsule was exposed and incised. To improve exposure of the medial meniscus, the medial collateral ligament (MCL) was elevated in subperiosteal fashion from its attachment on the proximal tibia. The medial meniscus was then exposed with flexion, external rotation, and valgus stress to the knee. Then, 4 mm diameter full-thickness cylindrical defects were created at the anterior horn of the medial meniscus by using Acufex® MosaicPlasty™ (Smith & Nephew Endoscopy, Andover, Massachusetts, USA) (Fig. 2a). The meniscus of the left knee ($n = 6$) was implanted with a TEC (Fig. 2b), while the right knee meniscus ($n = 6$) had no treatment (Fig. 2c).

The joint capsule was then repaired by suturing to the dissected MCL and wound closure in layers. Postoperative care, medications, and dressings were as previously described [39]. All the animals were cast immobilized at the hind limbs for 1 week, and then were returned to free cage activity. All the animals were sacrificed under anesthesia at 6 months after implantation surgery.

2.7. Morphological and histological evaluation of menisci

Following tissue harvest, the meniscal samples were examined grossly and photographed. The contact or separation of the lesion margins was assessed from both the femoral and tibial sides of the meniscus for all samples to ascertain any macroscopic evidence for macroscopic repair by a blinded experienced observer. For histological evaluation, tissue was fixed with 4% paraformaldehyde in phosphate buffer (pH 7.4), embedded in paraffin, and 4 μm sections were prepared. The sections were stained with hematoxylin and eosin (H&E) or Safranin O. Four to five serial transverse sections through the entire length of the tear were prepared from each meniscus sample. The stained sections were evaluated by a blinded experienced observer.

2.8. Histomorphometric assessment of menisci

All histological sections were photographed with a low magnification lens (2×) at the intersection of each lesion margin. They were then digitized, and histomorphometric analysis was performed with WinRooF (MITANI CO., Fukui, Japan). When the entire lesion overextended the image frames, a computerized assembling of multiple images was performed with the WinRooF program to obtain a single digitized image per histological section. Four to five serial transverse sections through the entire length of the defects were used for histomorphometric analysis. The ratio of the area of the repair tissue to that of the defect area, which was delineated by the margin of the adjacent meniscus, was calculated as the percentage of tissue repair. The entire length of the lesion interface was measured with a cursor led by the computer mouse. Subsequently, the zone of the lesion that achieved microscopic repair was assessed. It was considered as "integrated" if there was microscopic approximation and integration of the two tissues (repair and original). All data were recorded by a computer, and the percentage of each zone that achieved complete integration with respect to the entire interface of the lesion was calculated as percentage of integration [41].

2.9. Macroscopic evaluation of articular cartilage integrity facing the meniscal lesions

The degree of chondral damage in the femoral chondyle and tibial plateau regions was macroscopically evaluated according to the International Cartilage Repair Society (ICRS) scoring system (www.cartilage.org) as follows: grade 0, normal intact cartilage; grade I, chondral softening and blistering, superficial lesions; grade II, fraying, lesions and fissures extending down to <50% of cartilage depth; grade III, partial loss of cartilage thickness, cartilage lesions extending down to >50% of cartilage depth, as well as down to the calcified layer; grade IV, full-thickness cartilage loss with exposure of the subchondral bone. In addition, the macroscopic area of chondral lesions on the medial tibial plateau was measured by Image ver. 1.44 (National Institute of Health, Bethesda, USA).

2.10. Statistical analyses

All results are reported as mean ± S.D. Comparisons were evaluated by Wilcoxon's signed-rank test or unpaired Student's *t*-test on original numerical data. In all cases, $p < 0.05$ was considered statistically significant.

3. Results

3.1. In vitro fibro-chondrogenic differentiation

Since menisci are composed of fibro-cartilaginous tissue, a tissue which has characteristics intermediate between hyaline cartilage

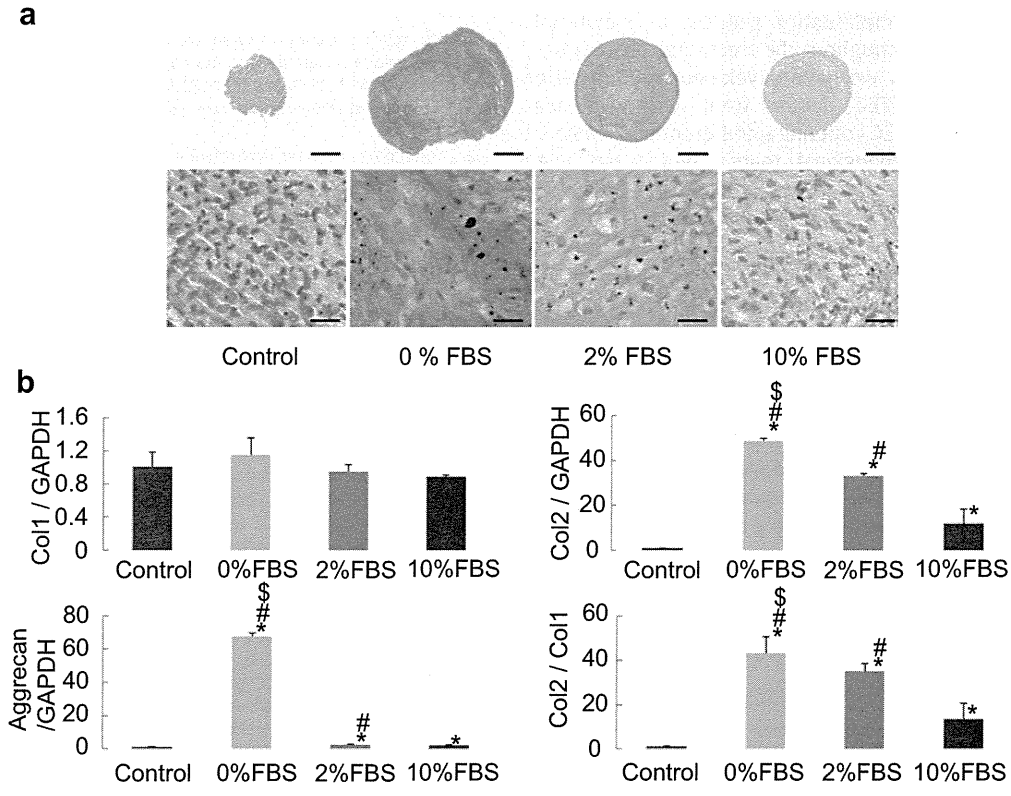

Fig. 1. *In vitro* fibro-chondrogenic differentiation of MSCs (a) Alcian blue staining of pellet cultures. The cell pellets were cultured in chondrogenic culture medium that contained HG-DMEM with 0 (0% FBS), 2 (2% FBS), or 10% (10% FBS) fetal bovine serum, as well as in control medium. Scale bars = 200 μm (upper) and 20 μm (bottom). (b) Quantitative RT-PCR analysis for collagen type 1, type 2, and aggrecan. Data are expressed as mean ± S.D. * denotes statistically significant difference compared with the control group ($p < 0.05$). # denotes statistically significant difference compared with the 10% FBS group ($p < 0.05$). $ denotes statistically significant difference compared with the 2% FBS group ($p < 0.05$).

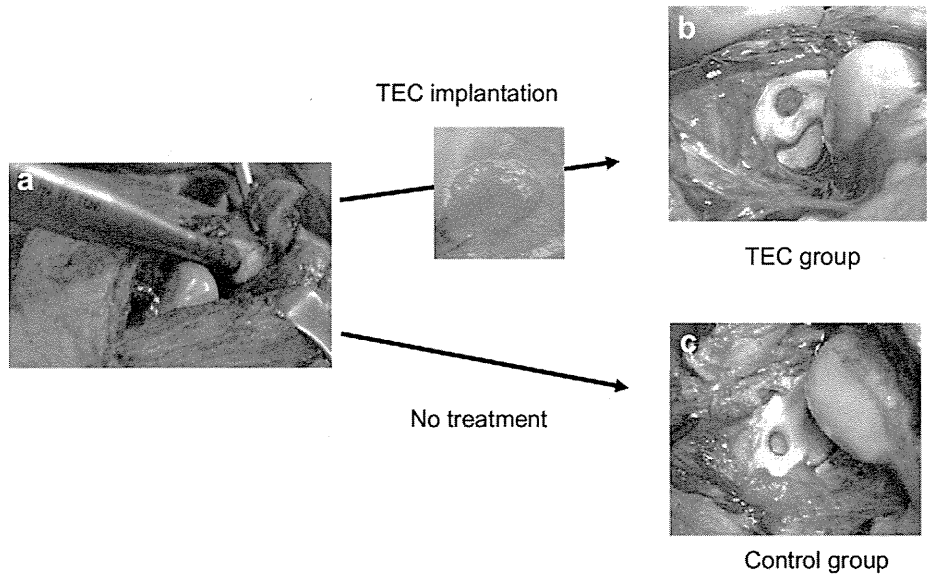

Fig. 2. Operative procedures. (a) A 4 mm diameter full-thickness cylindrical defect was created in the anterior horn of the medial meniscus. (b) TEC was implanted into the left knee defect, and (c) the right knee defect was left untreated.

and fibrous tissue, we first tested the *in vitro* differentiation capacity of the pellet-cultured synovial MSCs [42] to develop a fibro-cartilaginous tissue in the presence of different concentrations of FBS (from 0% to 10%) in the chondrogenic differentiation media.

The cell pellets responded differently according to the serum concentration used in the experiment. The size of the pellet, which has been shown to be an indicator of chondrogenic differentiation [42], was the largest and Alcian blue staining intensity was most strongly detected under the serum-free condition. The size of the pellet, as well as Alcian blue staining intensity decreased by the addition of serum in a dose-dependent manner (Fig. 1a, upper column). In the serum-free media, the rounded cells were scattered throughout the hyaline-like matrix with some rounded lacunae, which is a characteristic of chondrocytes (Fig. 1a, lower column). In the presence of 2% FBS, a fibrous matrix was more prominent in the pellet with moderate staining of Alcian blue staining further decreased (upper column) and the number of lacuna-positive cells decreased (lower column).

qRT-PCR analysis showed that the expression levels of cartilage marker genes, aggrecan and collagen II, were highest under serum-free conditions and their expression levels became reduced in reverse correlation with serum concentration. Conversely, the expression levels for the fibrous tissue marker gene, collagen I, were very consistent regardless of the concentration of serum. Accordingly, the ratio of collagen II to collagen I was inversely related to the serum concentration in a dose-dependent manner (Fig. 1b). Based on these results, it was concluded that the synovial MSCs in pellet culture could change the characteristics of the resultant cartilaginous tissues in which the ratio of hyaline- to fibro-cartilaginous tissue could be manipulated by altering the concentration of FBS in the chondrogenic culture medium.

3.2. Implantation of the TEC into meniscal defects in vivo

Defects (4 mm) were made in the medial menisci of miniature pigs and then either filled with a TEC or left untreated. At 6 months post-implantation, the control (untreated) defects were either not filled at all, or were partially filled with thin fibrous tissue, but even the latter contained empty areas as assessed by macroscopic observation (Fig. 3a). Thus, the defect model at the anterior horn of

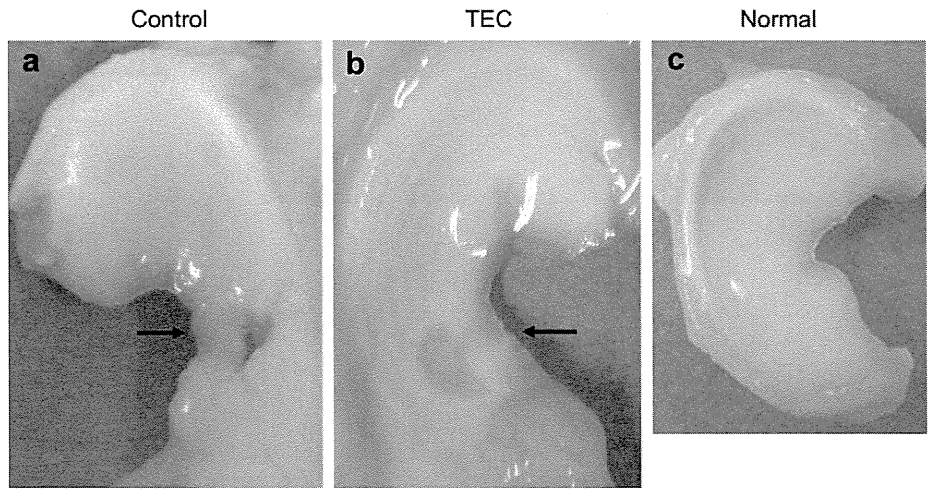

Fig. 3. Macroscopic assessment of whole menisci following harvest from animals at 6 months post-implantation. (a) The untreated (control) group, (b) the TEC-implanted group. Arrows show the initial meniscal defects. (c) A normal medial meniscus is shown for reference.

the medial meniscus was validated as a non-repairing by endogenous cells defect/lesion model. In contrast, the defects treated with a TEC were filled with repair tissue with good apparent integration to the adjacent host meniscus (Fig. 3b). Histological assessments confirmed that the control defects were either not repaired, or only partially repaired by fibrous tissue (Fig. 4a). Conversely, the defects treated with the TEC were securely filled with fibrous tissue with good tissue integration to the adjacent host meniscal body (Fig. 4b and d). Higher magnification views of the center of the reparative tissue revealed the presence of cartilage-like cells whose nuclei were in lacuna (arrows) within a dense fibrous tissue, suggesting the development of a fibro-cartilaginous repair tissue (Fig. 4e).

Histomorphometrical analysis also revealed that the meniscal defects treated with a TEC exhibited significantly better repair ratios than did the control defects (79.0 ± 3.5% *vs* 33.1 ± 10.1%; $p < 0.014$) (Fig. 4f), and that the integration ratio to adjacent host meniscal tissue was also significantly better in the defects treated with a TEC (82.7 ± 11.8% *vs* 51.1 ± 19.8%; $p < 0.026$) (Fig. 4g). Throughout the experiment, based on both macroscopic and microscopic assessment, no signs of infection or abnormal inflammatory response were observed within any of the knee joints of the miniature pigs used in this study.

3.3. TEC treatment and decreased meniscal body degeneration

The serial sections to those stained by hematoxylin & eosin (Fig. 4a–c) were stained by Safranin O which detects the localization of acidic proteoglycan that is contained in cartilaginous tissue (Fig. 5a–c). Safranin O staining was not detected in the repair tissue treated by the TEC (Fig. 5b), in contrast to the corresponding region in normal meniscus (Fig. 5c). However, it was notable that the central body of the control (untreated) menisci adjacent to the original defects had scarce or no staining with Safranin O (Fig. 5a arrows), while those of the TEC-treated menisci exhibited intense staining with Safranin O (Fig. 5b). The ratio of the Safranin O positive area within the central body of the meniscus adjacent to the original defect was significantly higher in the TEC-treated group than in the control group (62.0 ± 26.3% *vs* 11.2 ± 8.94%, $p = 0.030$) (Fig. 5d).

3.4. TEC treatment and development of chondral lesion in the femoral chondyle and tibial plateau regions

There were no chondral lesions detected at the time of implantation surgery. Conversely, by 6 months post-implantation,

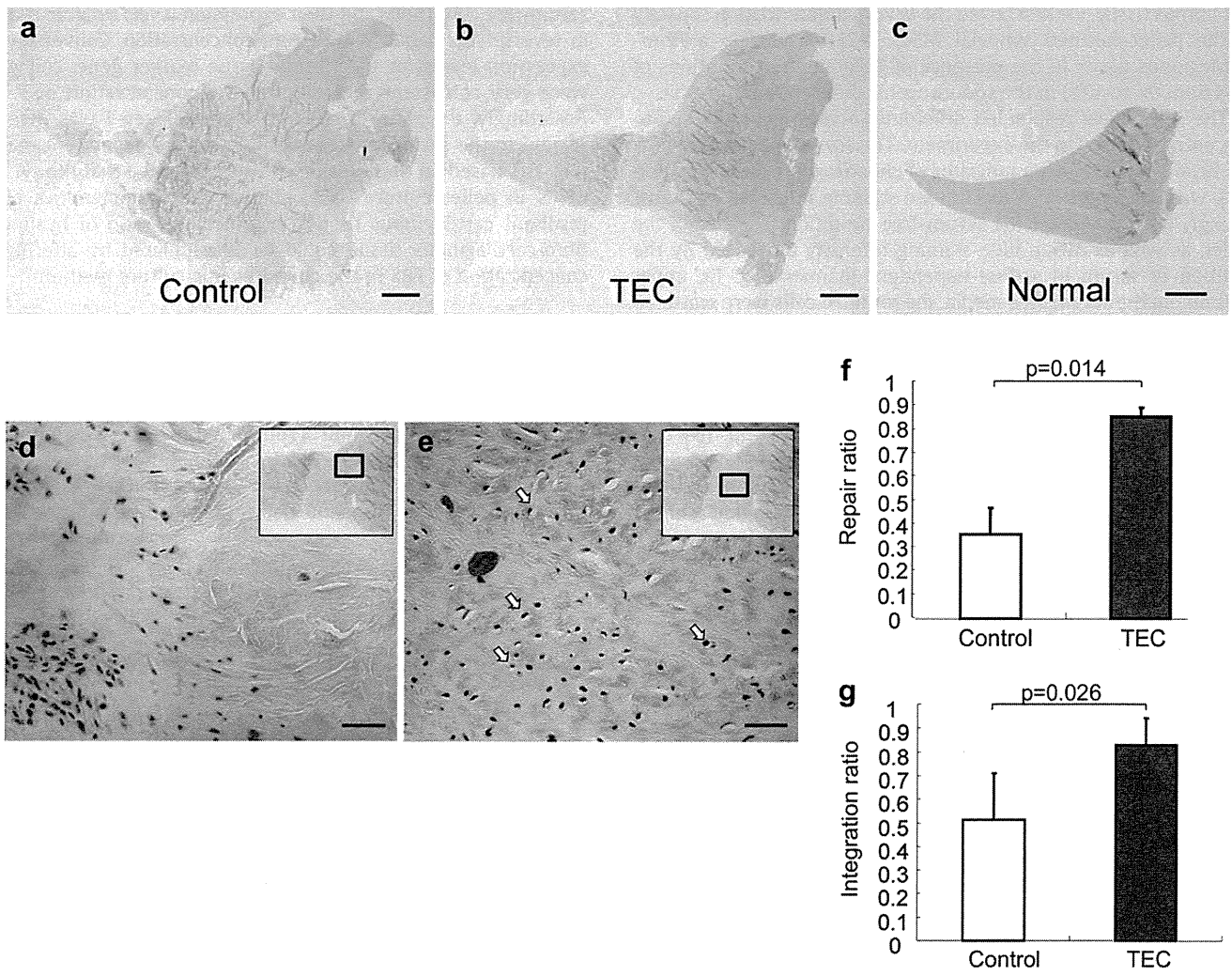

Fig. 4. Histology of whole sagittal sections of the medial meniscus stained with hematoxylin & eosin. (a) The untreated control group, (b) the TEC-treated group, and (c) normal meniscus for reference. Scale bars = 2000 μm. (d) Integration area of repair tissue to the native meniscal tissue. (e) Central area of repair tissue characterized by fibro-cartilaginous appearance with some rounded cells in lacuna (arrows). Scale bars = 40 μm (bottom). (f) Ratio of repair and (g) integration by histomorphometrical analysis. $p < 0.05$ *versus* the control group.

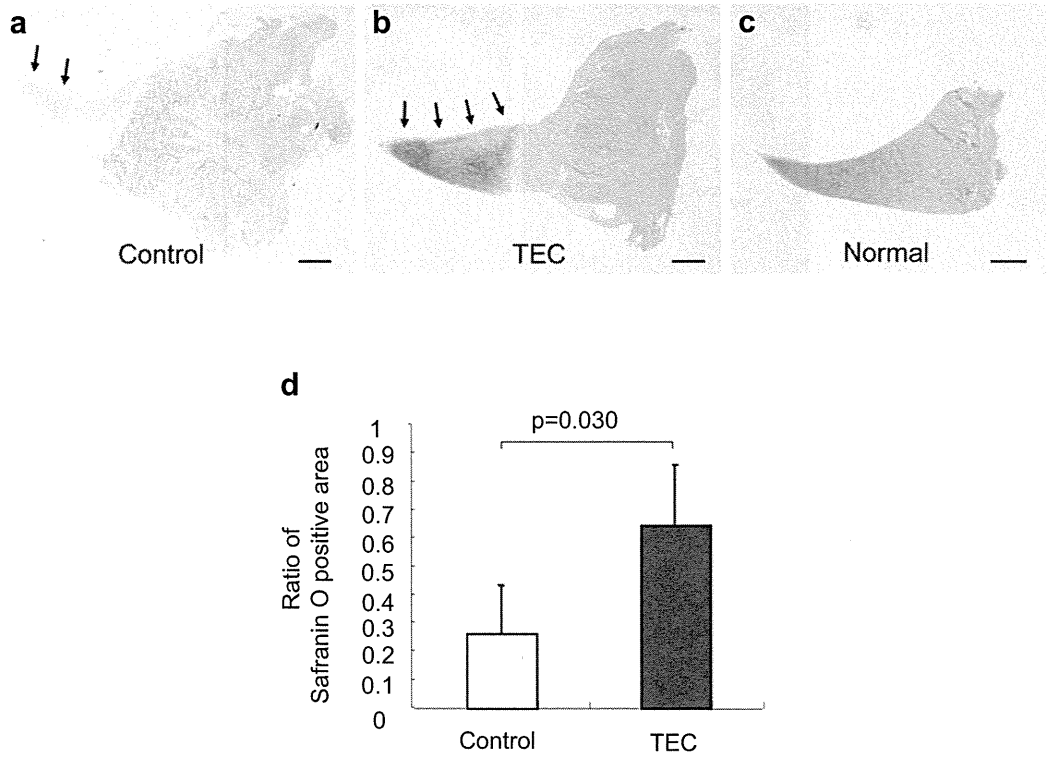

Fig. 5. Safranin O staining of whole sagittal sections of the medial meniscus. (a) The untreated control group, and (b) the TEC-treated group, and (c) normal meniscus. Note intense staining in the central body in the TEC-treated group while no staining in the untreated group (a, b, arrows). Scale bars = 2000 μm. (c) Ratio of Safranin O positive area within the central body of the meniscus adjacent to the original defect area. $p < 0.05$ *versus* the untreated control group.

focal articular lesions were observed on the tibial articular surfaces in all of the control knees ($n = 6$), and in 50% of the TEC-treated knees ($n = 3$) (Fig. 6a). The severity of tibial plateau chondral damage was macroscopically detectable. Based on the ICRS grading system, in the control group 2 knees had grade I lesions, 3 knees had grade II lesions, and 1 knee had grade III lesions. In contrast, in the TEC-treated group, 3 knees had grade 0 lesions and 3 knees had grade I lesions. The TEC-treated group had significantly lower grades of chondral lesions than did the control group ($p < 0.0163$) (Fig. 6b). Likewise, the area of the chondral lesions was significantly smaller in the TEC-treated group than the control group (5.67 ± 6.98 mm^2 *vs* 64.5 ± 43.0 mm^2, $p = 0.008$) (Fig. 6c). The cartilage from the femoral condyle region exhibited no apparent chondral damages both in the TEC-treated and control group (not shown).

4. Discussion

The optimal treatment of the injured meniscus may be facilitated by repairing the lesions/defects with fibro-cartilaginous tissue which has mixed characteristics of both hyaline cartilage and fibrous tissue. Based on their multipotent differentiation capacity, mesenchymal stem cell (MSC)-based therapy may have good potential to repair the injured meniscus with such a fibro-cartilaginous tissue. The present study revealed that the presence of serum could manipulate the phenotype of cartilaginous tissue from hyaline to fibrous. A fundamental difference between hyaline cartilage and fibro-cartilage, and one by which they can be defined, is the amount of the three important matrix: collagen I, collagen II and the proteoglycan aggrecan [43]. In the present study, the serum concentration negatively affected the aggrecan content and the collagen II/I expression ratio in a dose-dependent manner. These results may imply that MSCs would have the potential to differentiate towards various types of cartilage from hyaline- to fibro-cartilage in response to serum-related growth factors, and thus could validate the use of MSCs for the repair of the meniscus which is composed primarily of fibro-cartilage.

To investigate this potential in more detail, we used a large animal model with miniature pigs, which could subsequently allow the ready translation of the results to clinical applications based on the similarity of pigs to humans in terms of vascularization patterns, cell density, collagen structures, biomechanical properties, and weight [23,41,44–46]. Moreover, this sharing of many physiological similarities with humans indicates the miniature pig could be an optimal breed/species for preclinical experimentation [47]. Furthermore, the 4 mm diameter cylindrical defect model was revealed not to effectively heal spontaneously and thus, has been validated to test the efficacy of cell-based therapies.

Using this injury model, the present study showed that TEC derived from synovial membrane-derived MSCs can effectively repair such meniscal lesions/defects. Although the potential plasticity of MSCs has been confirmed in studies of *in vitro* chondrogenic differentiation in the present studies, the undifferentiated TEC were implanted as in our previous studies in order to maximize its tissue adhesiveness and enable the secure placement in the knee joints [28,39]. Without the addition of any specific growth factors such as BMP2, the TEC-mediated repair tissue exhibited fibro-cartilaginous tissue characteristics by 6 months post-implantation. The meniscus is consistently under unique loading conditions, namely a mixture of both tensile and compressive loading. Furthermore, the meniscus has poor vascularity in the central and inner body of the tissue. Taken together, the implanted TEC appears to have responded *in vivo* to such a unique biological and mechanical environment, leading to the effective development of a fibro-cartilaginous tissue in the damaged menisci.

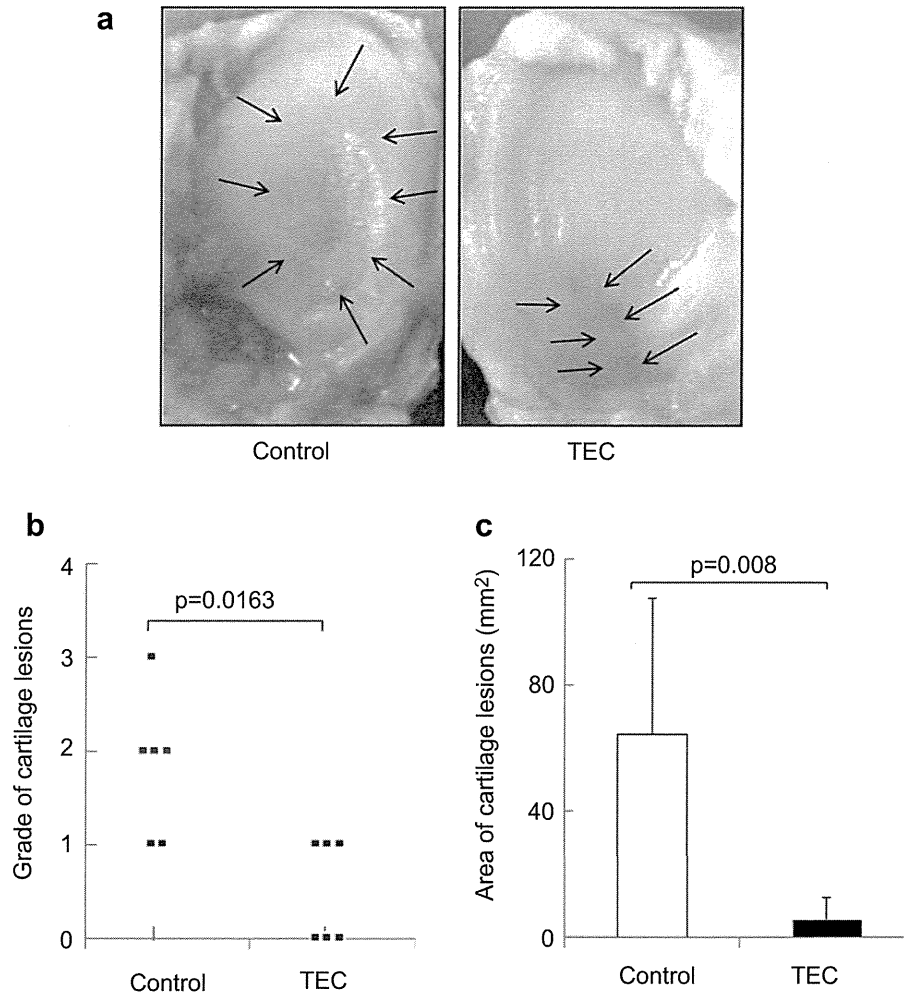

Fig. 6. Post-traumatic chondral lesions on the tibial plateau. (a) Macroscopic findings of tibial chondral damage associated with meniscal lesions at 6 months post-implantation (arrows). (b) Grading of chondral lesions based on International Cartilage Repair Society Scores, and (c) quantification of chondral lesion areas. $p < 0.05$ *versus* the untreated control group.

Similar to previous studies investigating articular cartilage repair in a porcine model [41,44], the implantation without fixation of TEC generated from synovial membrane-derived MSCs also promoted repair with good integration to the adjacent host meniscal tissue. In spite of the fact that the injured meniscus is subjected to mechanically unstable conditions, tissue repair was attained in the present study following the simple implantation of the TEC without any reinforcement via tissue fixation, such as with a suture or via pin fixation. Such characteristics of these TEC could contribute to simplify the surgical procedures involved with reduced surgical duration, which is a clinically relevant variable.

It is notable that the menisci repaired by implantation of a TEC maintained the proteoglycans within the central body of the meniscus as indicated by the positive Safranin O staining. Conversely, significant losses of proteoglycan were observed in the untreated control group. To our knowledge, such an effect by meniscal repair on the maintenance of matrix composition within the adjacent meniscal body has not been demonstrated by any previous animal experiments. These results suggest that mechanical stabilization of the central meniscal body by the TEC may be beneficial for the prevention of further meniscal degeneration following the initial injury. Since the preservation of meniscus has a pivotal role in the prevention of osteoarthritis [48], such protective effects on the integrity of the matrix composition within the meniscal body could have significant clinical implications, particularly for younger patients at risk to develop osteoarthritis at an early age.

Moreover, meniscal repair following implantation of a TEC prevented, in large part, the development of secondary chondral damage in the tibial plateau associated with the meniscal injury. It should be noted that the quantitative evaluation of meniscal body degeneration and of collateral chondral damage was enabled by the use of this large animal model. Reproducible creation of specific meniscal defects in terms of size and location, as well as implantation surgery is required to validate the resultant quantitative evaluations and, in this regard, small animals such as rodents are not likely able to meet these requirements due to the limited size of their knee joints. As the major roles of meniscus are related to load absorption and distribution within the knee joint, such chondroprotective effects enhance the significance of meniscal repair using the TEC approach in the prevention of subsequent osteoarthritis.

In contrast with the case at the tibial plateau, the cartilage on the femoral condyle did not exhibit chondral damage, which was macroscopically detectable, suggesting the regional difference in the development of chondral damage following menical injury. A biomechanical study revealed that the cartilage at the tibial plateau has less stiffness than that at the femoral condyle [49].

Furthermore, a recent study using carrageenan-induced arthritis demonstrated that the cartilage tissue at the tibial plateau more sensitively responds to chemical stimulation than that at the femoral chondyle regarding the changes in cytokine and MMP expression [50]. Taken together, it is suggested that the cartilage at the tibial plateau might have inferior mechanical property and likely more sensitive to the factors to induce degenerative changes, and such difference might have related to the results in the present study.

Specifically related to clinical relevance, it should be pointed out that the present study was performed using allogenic MSCs. Similar to our previous experimental studies using the TEC approach for articular cartilage repair [28,39], no abnormal inflammatory reactions or obvious immunologic rejection were observed throughout the experiments as determined by histological assessment. It is widely accepted that MSCs do exhibit an immune-tolerance capacity [51–53]. The use of allogenic stem cells could be advantageous from a time- and cost-saving perspective, without sacrifice of host tissue in comparison with an autologous cell-based approach. Taken together, it is suggested that allogenic MSC-based therapies using the TEC approach may be advantageous for meniscal repair in a clinical setting.

With regard to potential limitations of the present study, firstly, we did not follow the fate of the implanted MSCs in the TECs within the knee joint. It is important to understand the fate of the implanted cells for elucidation of the mechanisms responsible for the tissue repair. Future studies will be required to address this limitation, possibly using a specific cell labeling method for this purpose. Furthermore, we did not obtain detailed mechanical data on the repair tissues [54–57]. This was due in part to difficulties in clamping the fragile tissue specimens to the available testing device (unpublished data). However, the results of the present study, including the prevention of subsequent meniscal body degeneration and of the development of associated chondral damage at the tibial plateau following TEC implantation, strongly suggest the "functional" recovery of the meniscus following implantation of the TEC. Thus, a lack of mechanical testing data could be compensated by the morphological assessments suggesting the 'functionality' of the repair tissue mediated by TEC implantation.

Finally, the studies presented assessed the meniscal repair tissue at 6 months post-implantation. Likely additional studies will have to be performed at longer time points post-implantation to assess whether the TEC approach yields long-term repair with or without continued improvement of the characteristics of the repair tissue.

5. Conclusions

The results of the present study suggest that TEC-based therapy for repair of meniscal lesions could help restore meniscal function, and furthermore, could have a preventive effect from subsequent development of post-traumatic arthritis within the knee joint.

Acknowledgements

This research was supported by a Grant-in-Aid for Scientific Research, Japan Society for the Promotion of Science (B) and New Energy and Industrial Technology Development Organization, Japan. DAH was supported by the AIHS Team Grant in Osteoarthritis Research.

Appendix A. Supplementary data

Supplementary data related to this article can be found at http://dx.doi.org/10.1016/j.biomaterials.2012.11.039.

References

[1] Rattner JB, Matyas JR, Barclay L, Holowaychuk S, Sciore P, Lo IK, et al. New understanding of the complex structure of knee menisci: implications for injury risk and repair potential for athletes. Scand J Med Sci Sports 2011;21:543–53.
[2] King D. The healing of semilunar cartilages. J Bone Joint Surg 1936;18:333–42.
[3] Levy IM, Torzilli PA, Gould JD, Warren RF. The effect of lateral meniscectomy on motion of the knee. J Bone Joint Surg Am 1989;71:401–6.
[4] Ahmed AM, Burke DL. In-vitro measurement of static pressure distribution in synovial joints – part I: tibial surface of the knee. J Biomech Eng 1983;105:216–25.
[5] Krause WR, Pope MH, Johnson RJ, Wilder DG. Mechanical changes in the knee after meniscectomy. J Bone Joint Surg Am 1976;58:599–604.
[6] Arnoczky SP, Warren RF. Microvasculature of the human meniscus. Am J Sports Med 1982;10:90–5.
[7] Henning CE, Lynch MA, Clark JR. Vascularity for healing of meniscus repairs. Arthroscopy 1987;3:13–8.
[8] Baratz ME, Fu FH, Mengato R. Meniscal tears: the effect of meniscectomy and of repair on intraarticular contact areas and stress in the human knee. A preliminary report. Am J Sports Med 1986;14:270–5.
[9] Fukubayashi T, Kurosawa H. The contact area and pressure distribution pattern of the knee. A study of normal and osteoarthrotic knee joints. Acta Orthop Scand 1980;51:871–9.
[10] Voloshin AS, Wosk J. Shock absorption of meniscectomized and painful knees: a comparative in vivo study. J Biomed Eng 1983;5:157–61.
[11] LeRoux MA, Arokoski J, Vail TP, Guilak F, Hyttinen MM, Kiviranta I, et al. Simultaneous changes in the mechanical properties, quantitative collagen organization, and proteoglycan concentration of articular cartilage following canine meniscectomy. J Orthop Res 2000;18:383–92.
[12] Sprinz R. The role of the meniscus in the healing process, following excision of the articular surfaces of the mandibular joint in rabbits. J Anat 1963;97:345–52.
[13] Ehrlich MG, Mankin HJ, Jones H, Grossman A, Crispen C, Ancona D. Biochemical confirmation of an experimental osteoarthritis model. J Bone Joint Surg Am 1975;57:392–6.
[14] Elmer RM, Moskowitz RW, Frankel VH. Meniscal regeneration and post-meniscectomy degenerative joint disease. Clin Orthop Relat Res 1977:304–10.
[15] Heatley FW. The meniscus – can it be repaired? An experimental investigation in rabbits. J Bone Joint Surg Br 1980;62:397–402.
[16] Paatsama S. The structure and histopathology of the canine meniscus. Am J Vet Res 1954;15:495–9.
[17] Cox JS, Nye CE, Schaefer WW, Woodstein IJ. The degenerative effects of partial and total resection of the medial meniscus in dogs' knees. Clin Orthop Relat Res 1975:178–83.
[18] Little CB, Ghosh P, Bellenger CR. Topographic variation in biglycan and decorin synthesis by articular cartilage in the early stages of osteoarthritis: an experimental study in sheep. J Orthop Res 1996;14:433–44.
[19] Lutfi AM. Morphological changes in the articular cartilage after meniscectomy. An experimental study in the monkey. J Bone Joint Surg Br 1975;57:525–8.
[20] Lynch MA, Henning CE, Glick Jr KR. Knee joint surface changes. Long-term follow-up meniscus tear treatment in stable anterior cruciate ligament reconstructions. Clin Orthop Relat Res 1983:148–53.
[21] Roos H, Lauren M, Adalberth T, Roos EM, Jonsson K, Lohmander LS. Knee osteoarthritis after meniscectomy: prevalence of radiographic changes after twenty-one years, compared with matched controls. Arthritis Rheum 1998;41:687–93.
[22] Andersson-Molina H, Karlsson H, Rockborn P. Arthroscopic partial and total meniscectomy: a long-term follow-up study with matched controls. Arthroscopy 2002;18:183–9.
[23] Weinand C, Peretti GM, Adams Jr SB, Randolph MA, Savvidis E, Gill TJ. Healing potential of transplanted allogeneic chondrocytes of three different sources in lesions of the avascular zone of the meniscus: a pilot study. Arch Orthop Trauma Surg 2006;126:599–605.
[24] Hickery MS, Bayliss MT, Dudhia J, Lewthwaite JC, Edwards JC, Pitsillides AA. Age-related changes in the response of human articular cartilage to IL-1alpha and transforming growth factor-beta (TGF-beta): chondrocytes exhibit a diminished sensitivity to TGF-beta. J Biol Chem 2003;278:53063–71.
[25] Mesiha M, Zurakowski D, Soriano J, Nielson JH, Zarins B, Murray MM. Pathologic characteristics of the torn human meniscus. Am J Sports Med 2007;35:103–12.
[26] Pittenger MF, Mackay AM, Beck SC, Jaiswal RK, Douglas R, Mosca JD, et al. Multilineage potential of adult human mesenchymal stem cells. Science 1999;284:143–7.
[27] Krebsbach PH, Kuznetsov SA, Bianco P, Robey PG. Bone marrow stromal cells: characterization and clinical application. Crit Rev Oral Biol Med 1999;10:165–81.
[28] Shimomura K, Ando W, Tateishi K, Nansai R, Fujie H, Hart DA, et al. The influence of skeletal maturity on allogenic synovial mesenchymal stem cell-based repair of cartilage in a large animal model. Biomaterials 2010;31:8004–11.
[29] De Bari C, Dell'Accio F, Tylzanowski P, Luyten FP. Multipotent mesenchymal stem cells from adult human synovial membrane. Arthritis Rheum 2001;44:1928–42.

[30] Sakaguchi Y, Sekiya I, Yagishita K, Muneta T. Comparison of human stem cells derived from various mesenchymal tissues: superiority of synovium as a cell source. Arthritis Rheum 2005;52:2521–9.
[31] Arnoczky SP, Warren RF. The microvasculature of the meniscus and its response to injury. An experimental study in the dog. Am J Sports Med 1983; 11:131–41.
[32] Horie M, Sekiya I, Muneta T, Ichinose S, Matsumoto K, Saito H, et al. Intra-articular injected synovial stem cells differentiate into meniscal cells directly and promote meniscal regeneration without mobilization to distant organs in rat massive meniscal defect. Stem Cells 2009;27:878–87.
[33] Mizuno K, Muneta T, Morito T, Ichinose S, Koga H, Nimura A, et al. Exogenous synovial stem cells adhere to defect of meniscus and differentiate into cartilage cells. J Med Dent Sci 2008;55:101–11.
[34] Pereira H, Frias AM, Oliveira JM, Espregueira-Mendes J, Reis RL. Tissue engineering and regenerative medicine strategies in meniscus lesions. Arthroscopy 2011;27:1706–19.
[35] Daniels AU, Andriano KP, Smutz WP, Chang MK, Heller J. Evaluation of absorbable poly(ortho esters) for use in surgical implants. J Appl Biomater 1994;5:51–64.
[36] van der Elst M, Klein CP, de Blieck-Hogervorst JM, Patka P, Haarman HJ. Bone tissue response to biodegradable polymers used for intra medullary fracture fixation: a long-term in vivo study in sheep femora. Biomaterials 1999;20: 121–8.
[37] Yang C, Hillas PJ, Baez JA, Nokelainen M, Balan J, Tang J, et al. The application of recombinant human collagen in tissue engineering. BioDrugs 2004;18: 103–19.
[38] Martin MJ, Muotri A, Gage F, Varki A. Human embryonic stem cells express an immunogenic nonhuman sialic acid. Nat Med 2005;11:228–32.
[39] Ando W, Tateishi K, Hart DA, Katakai D, Tanaka Y, Nakata K, et al. Cartilage repair using an in vitro generated scaffold-free tissue-engineered construct derived from porcine synovial mesenchymal stem cells. Biomaterials 2007;28: 5462–70.
[40] Ando W, Tateishi K, Katakai D, Hart DA, Higuchi C, Nakata K, et al. In vitro generation of a scaffold-free tissue-engineered construct (TEC) derived from human synovial mesenchymal stem cells: biological and mechanical properties and further chondrogenic potential. Tissue Eng Part A 2008;14:2041–9.
[41] Peretti GM, Gill TJ, Xu JW, Randolph MA, Morse KR, Zaleske DJ. Cell-based therapy for meniscal repair: a large animal study. Am J Sports Med 2004;32: 146–58.
[42] Sekiya I, Vuoristo JT, Larson BL, Prockop DJ. In vitro cartilage formation by human adult stem cells from bone marrow stroma defines the sequence of cellular and molecular events during chondrogenesis. Proc Natl Acad Sci U S A 2002;99:4397–402.
[43] Freemont AJ, Hoyland J. Lineage plasticity and cell biology of fibrocartilage and hyaline cartilage: its significance in cartilage repair and replacement. Eur J Radiol 2006;57:32–6.
[44] Dutton AQ, Choong PF, Goh JC, Lee EH, Hui JH. Enhancement of meniscal repair in the avascular zone using mesenchymal stem cells in a porcine model. J Bone Joint Surg Br 2010;92:169–75.
[45] Chevrier A, Nelea M, Hurtig MB, Hoemann CD, Buschmann MD. Meniscus structure in human, sheep, and rabbit for animal models of meniscus repair. J Orthop Res 2009;27:1197–203.
[46] Ghadially FN, Wedge JH, Lalonde JM. Experimental methods of repairing injured menisci. J Bone Joint Surg Br 1986;68:106–10.
[47] Vodicka P, Smetana Jr K, Dvorankova B, Emerick T, Xu YZ, Ourednik J, et al. The miniature pig as an animal model in biomedical research. Ann N Y Acad Sci 2005;1049:161–71.
[48] Koski JA, Ibarra C, Rodeo SA, Warren RF. Meniscal injury and repair: clinical status. Orthop Clin North Am 2000;31:419–36.
[49] Lyyra T, Kiviranta I, Vaatainen U, Helminen HJ, Jurvelin JS. In vivo characterization of indentation stiffness of articular cartilage in the normal human knee. J Biomed Mater Res 1999;48:482–7.
[50] Achari Y, Reno CR, Frank CB, Hart DA. Carrageenan-induced transient inflammation in a rabbit knee model: molecular changes consistent with an early osteoarthritis phenotype. Inflamm Res 2012;61:907–14.
[51] Nauta AJ, Fibbe WE. Immunomodulatory properties of mesenchymal stromal cells. Blood 2007;110:3499–506.
[52] Rasmusson I. Immune modulation by mesenchymal stem cells. Exp Cell Res 2006;312:2169–79.
[53] Nasef A, Ashammakhi N, Fouillard L. Immunomodulatory effect of mesenchymal stromal cells: possible mechanisms. Regen Med 2008;3:531–46.
[54] Pabbruwe MB, Kafienah W, Tarlton JF, Mistry S, Fox DJ, Hollander AP. Repair of meniscal cartilage white zone tears using a stem cell/collagen-scaffold implant. Biomaterials 2010;31:2583–91.
[55] Nerurkar NL, Han W, Mauck RL, Elliott DM. Homologous structure-function relationships between native fibrocartilage and tissue engineered from MSC-seeded nanofibrous scaffolds. Biomaterials 2011;32:461–8.
[56] Hennerbichler A, Moutos FT, Hennerbichler D, Weinberg JB, Guilak F. Repair response of the inner and outer regions of the porcine meniscus in vitro. Am J Sports Med 2007;35:754–62.
[57] McNulty AL, Moutos FT, Weinberg JB, Guilak F. Enhanced integrative repair of the porcine meniscus in vitro by inhibition of interleukin-1 or tumor necrosis factor alpha. Arthritis Rheum 2007;56:3033–42.

Bone 52 (2013) 659–667

Contents lists available at SciVerse ScienceDirect

Bone

journal homepage: www.elsevier.com/locate/bone

Original Full Length Article

Design and optimization of the oriented groove on the hip implant surface to promote bone microstructure integrity

Yoshihiro Noyama [a,b], Takayoshi Nakano [a,*], Takuya Ishimoto [a], Takashi Sakai [c], Hideki Yoshikawa [c]

[a] Division of Materials and Manufacturing Science, Graduate School of Engineering, Osaka University, 2-1 Yamada-oka, Suita, Osaka 565-0871, Japan
[b] Department of Research and Development Division, Nakashima Medical Co., Ltd., 688-1 Joto-Kitakata, Higashi-ku, Okayama, Okayama 709-0625, Japan
[c] Department of Orthopedic Surgery, Osaka University Graduate School of Medicine, 2-2 Yamada-oka, Suita, Osaka 565-0871, Japan

ARTICLE INFO

Article history:
Received 7 August 2012
Revised 4 November 2012
Accepted 5 November 2012
Available online 10 November 2012

Edited by: Thomas Einhorn

Keywords:
Hip stem
Stress shielding
Finite element analysis (FEA)
Principal stress
Oriented groove
Biological apatite (BAp) alignment

ABSTRACT

We proposed a novel surface modification for an artificial hip joint stem from the viewpoint of maintenance and establishment of appropriate bone function and microstructure, represented by the preferred alignment of biological apatite (BAp) and collagen (Col). Oriented grooves were introduced into the proximal medial region of the femoral stem to control the principal stress applied to the bone inside the grooves, which is a dominant factor contributing to the promotion of Col/BAp alignment. The groove angle and the stem material were optimized based on the stress inside the grooves through a finite element analysis (FEA). Only the groove oriented proximally by 60° from the normal direction of the stem surface generated the healthy maximum principal stress distribution. The magnitude of the maximum principal stress inside the groove decreased with increasing the stem Young's modulus, while the direction of the stress did not largely changed. An *in vivo* implantation experiment showed that this groove was effective in inducing the new bone with preferential Col/BAp alignment along the groove depth direction which corresponded to the direction of maximum principal stress inside the groove. The anisotropic principal stress distribution and the oriented microstructure inside the groove are similar to those found in the femoral trabeculae; therefore, the creation of the oriented groove is a potent surface modification for optimizing implant design for a long-term fixation.

Introduction

The number of total hip replacements (THRs) has increases every year, and in the United States, nearly 231,000 THRs were reported in 2006 [1]. In recent years, THRs are increasingly performed on younger patients [2], and the ratio of the number of revision hip replacements to primary hip replacements is as high as 20% [3]. According to the results of a US epidemiological study that examined the factors contributing to revision hip replacements, Bozic et al. [4] reported that 24.7% of the revisions were due to mechanical loosening of the femoral component; 18.7% were due to periprosthetic fractures, both of which are thought to be induced by bone loss due to a stress shielding [5,6]. The stress shielding refers to inhibition of the transfer of physiological stress to bone tissues due to a difference between Young's modulus (YM) of the bone and that of the implant. Meanwhile, only 8.6% of the revisions were caused by implant failures [4], indicating high mechanical reliability of artificial hip joint implants themselves. The degradation of the bone tissues surrounding the femur and decrease in bone mechanical functions can lead to revision hip replacement. Prevention of such events requires an implant design that supports the microstructural and mechanical health of the bone surrounding the implant, rather than an improvement of the implant material itself.

Microstructure of bone materials, independent of bone mass and bone mineral density (BMD) [7,8], is an important factor in the assessment of bone health. The *c*-axis alignment of biological apatite (BAp) strongly contributes to bone mechanical functions, because BAp has a hexagonal-base crystal structure and shows marked mechanical anisotropy along the *a*- and *c*-axes. YM is significantly higher in the direction of the *c*-axis than in direction of the *a*-axis [9], and because the *c*-axis alignment of BAp in the bone is nearly identical to the direction of the extension of the Col fibril [10,11], the mechanical function of bone as a Col/BAp complex can display anisotropy depending on the degree of preferential alignment [12,13]. It is recently demonstrated that the degree of BAp *c*-axis alignment rather than BMD determines YM measured by nanoindentation along the direction parallel to the BAp alignment direction [14]. The maximum principal stress distribution loaded on the bone *in vivo* seems to be one of the vital contributory factors of the BAp alignment. As shown by Nakano et al. [8], along with the *in vivo* stress changes, the BAp alignment depends strongly on the bone site, such as the long bones, the skull bone, and the mandible bone. For example, in the cortical bone of a mature monkey mandible, the *c*-axis of BAp

* Corresponding author at: 2-1 Yamada-oka, Suita, Osaka 565-0871, Japan. Fax: +81 6 6879 7505.
E-mail addresses: y-noyama@nakashima.co.jp (Y. Noyama), nakano@mat.eng.osaka-u.ac.jp (T. Nakano), ishimoto@mat.eng.osaka-u.ac.jp (T. Ishimoto), tsakai@ort.med.osaka-u.ac.jp (T. Sakai), yhideki@ort.med.osaka-u.ac.jp (H. Yoshikawa).

8756-3282/$ – see front matter © 2012 Elsevier Inc. All rights reserved.
http://dx.doi.org/10.1016/j.bone.2012.11.005

is uniaxially, mesiodistally aligned. However, the alignment direction near the teeth changes, becoming parallel to the biting direction. *In vivo* BAp alignment sensitively changes in response to the direction and magnitude of localized stress, such as mastication stress. Bone can improve its mechanical function by altering BAp alignment in the direction of the maximum principal stress, and such a phenomenon can be found not only in cortical bone, but also in the trabecular bone.

The trabecular bone is in direct contact with the implant, in cementless artificial hip joints. Therefore, trabecular bone is a site responsible for load transfer and bone-implant bonding. According to Wolff's law, trabecular bones exhibit a characteristic pattern along the principal stress direction, and the trabecular pattern is restructured as a result of changes in principal stress distribution due to trauma or changes in life pattern [15,16]. Furthermore, inside each individual trabecular bone, the BAp *c*-axis preferentially aligns along the direction of the trabeculae [17], which makes the trabecula mechanically anisotropic [18]. Thus, in the healthy trabecular bone, the principal stress direction corresponds to trabecular direction, which may be a goal to achieve the formation of appropriate Col/BAp alignment and resultant mechanical performance even after the implantation of a stem.

Since the Col/BAp alignment can be one of the indices of mechanical bone health, making it a focus may allow optimization of these implants [19], so that by vitalizing microstructure and mechanical function of the bone around the implant, new artificial hip joints can be designed to allow the implant to induce principal stress distribution suitable to the surrounding bone along with a BAp structure that is aligned similarly to that of normal bones. In this study, we propose an oriented groove structure in the medial part of the proximal region of the femoral stem. The trabecular bones in the proximal medial region of the femur are called a secondary compressive group consisting of trabeculae extending proximally toward the greater trochanter. Since this region contributes significantly to implant anchorage in cementless artificial hip joints [20], the induction of tissues with a healthy, aligned BAp structure is a pivotal strategy.

Previous attempts to make the stem surface porous were performed to fixate implants at the proximal medial region of the femur [21–23]. However, the conformations of the pores introduced using conventional fabrication methods were three-dimensionally (3D) isotropic, and in most cases, their purpose was to simply achieve anchoring through formation of new bone tissue inside the pores [23]. Recently, it was reported that even though porous (Ti mesh)-coated cementless Ti–6Al–4V stem was applied into human femur, stress shielding occurred leading to bone loss and degradation of BAp alignment in the femur surrounding the stem [24]. This suggests that new strategy for designing implant is needed aiming at avoiding stress shielding and aggressively controlling the stress distribution around the implant. At present, we do not know of any other implant surface design that accounts for the control of the principal stress distribution and subsequent creation of healthy Col/BAp alignment.

In this study, we hypothesized that anisotropic pores (grooves) introduced onto the surface of an artificial hip joint stem would induce maximum principal stress along the groove depth, which would further stimulate formation of new bone with the suitable preferential alignment of Col/BAp. To test this hypothesis, finite element analysis (FEA) was conducted to examine the effects of anisotropic grooves on the maximum principal stress distribution generated in the grooves, followed by *in vivo* implantation experiment in beagles for exploring the creation of Col/BAp alignment in the newly formed bone inside the grooves. Finally, we proposed a guideline for designing optimized implants that allow control of the maximum principal stress by the groove and the resultant Col/BAp alignment.

Materials and methods

A beagle femur was used as a model for the optimized design of an artificial hip joint stem. An FEA was used for predicting principal stress generated in the anisotropic grooves. An animal implantation test was performed to examine establishment of the Col/BAp alignment in the bone formed inside the grooves. The predicted stress and the Col/BAp alignment were compared to derive an optimized surface design for an artificial hip joint stem.

Construction of the analytical model

For FEA analysis, 3D models of the beagle femur and the artificial hip joint stem were modeled separately. The intact right femur of a beagle (age: 2 years, weight: 13.0 kg) was extracted, and tomographic images with a resolution of 90 μm × 90 μm × 90 μm were obtained at 1-mm intervals along the femoral axis, using micro-focus X-ray computed tomography (μCT; SMX-100CT, Shimadzu, Japan), with a tube voltage of 65 kV, and a tube current of 27 μA.

To prepare an FEA model, the outline of the cortical bone was extracted after binarization of all tomographic images using CT image analysis software (Mimics 11, Materialise, Belgium). Procedures, such as spline interpolation, were performed from the stacked contours using a 3D surface modeling software (Imageware 10, Siemens, USA). Using these resources, a 3D model of the femur was constructed [25].

The stem was designed so that the cross-section from the femoral neck to the distal end was rectangular to preserve trabecular bone and marrow and minimize impairment of blood flow in the cortical bone [26,27]. The medial–lateral surface was tapered. While the features and dimensions needed for the design were measured based on a femur model, a femoral stem with an outer configuration similar to that shown in Fig. 1C was modeled using 3D CAD software (UGNX 4, Siemens, USA).

Introduction of the oriented groove on the stem surface

An oriented groove structure for controlling stress distribution was introduced to the proximal medial region of the femoral stem. To analyze the groove angle dependence on the principal stress distribution inside the groove, 5 groove angles were used, 60°, 30°, 0°, −30°, and −60°, with the proximal side as the positive direction compared to the normal direction of the stem surface (Fig. 1A). A pore diameter of several hundred microns is considered optimal for the migration of osteoblasts and the formation of mineralized tissue [28,29]. Therefore, for all cases, the groove width was set to 500 μm and the groove depth to 1 mm (Fig. 1B).

The artificial hip joint was inserted into the marrow cavity of the beagle femur model (Fig. 1C) using 3D imaging so that the groove that was introduced into the femoral stem surface was located approximately at the level of the lesser trochanter. The second compressive group that is dominantly subjected to compressive stress is present in this region.

Setting the FEA conditions

Three materials were defined on the bone-implant model: the femoral stem region, the cortical bone region, and the trabecular bone region or the interior of the groove cavity (Figs. 1A, C), and an analysis model was prepared using a finite element pre-processor (HyperMesh 9; Altair Engineering, USA). As shown in Fig. 1, the tetrahedral primary element with a dimension of 500 μm was used: the number of elements was 48,170, and the number of nodes was 592,088. To examine the effect of element dimension on the resultant principal stress distribution, we applied a small element (62.5 μm in dimension) to the 60° groove and calculated principal stress. As a result, slightly disordered principal stress direction was found near the stem surface, but there was little effect on the quantitative analysis. Therefore, the element 500 μm in dimension was used for all FEA calculation.

The loading conditions were based on the method described by Rietbergen et al. [30], as shown in Fig. 1C. The force applied on the

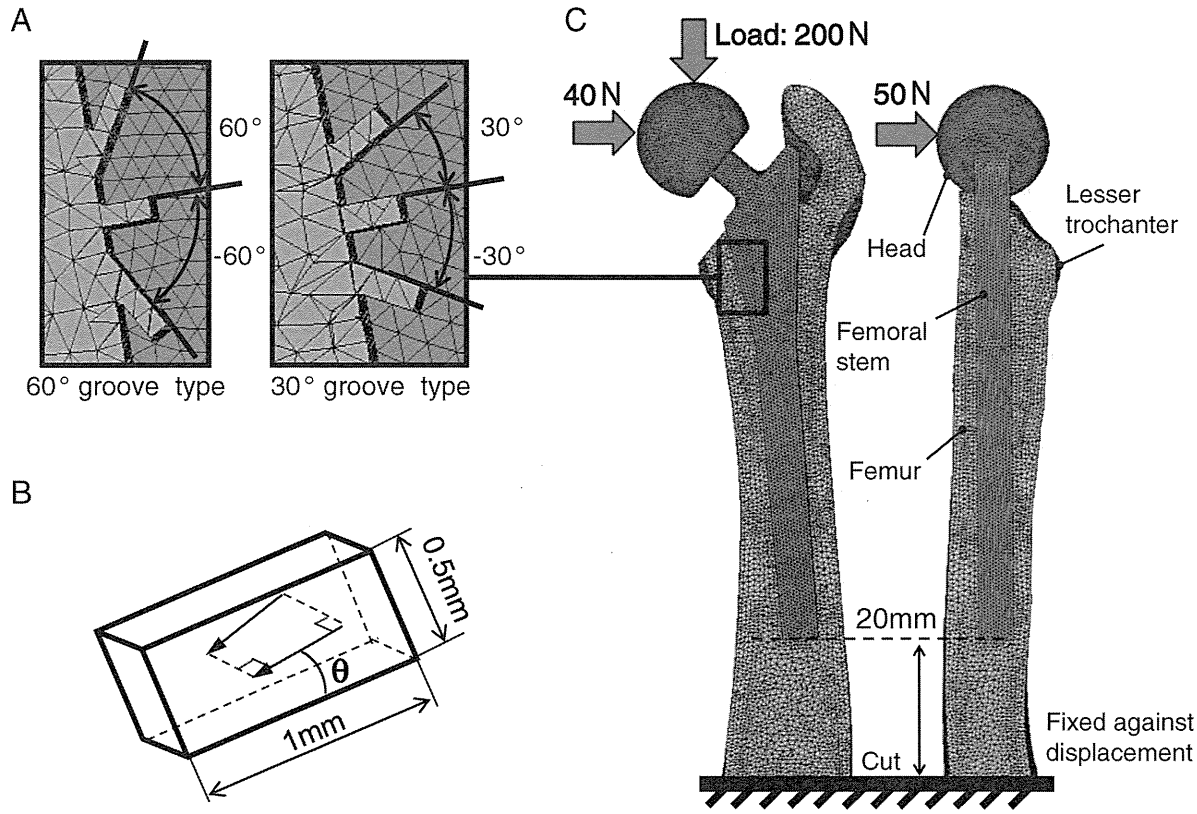

Fig. 1. 3D FEA model of the beagle femur–artificial hip joint implant used in this study. (A) Two types of groove angle combinations on the surface of the proximal medial region of the femoral stem: (60°/0°/−60°) groove and (30°/0°/−30°) groove. (B) Definition of the angle, θ, between groove wall and the maximum principal stress direction in the groove. (C) Loading and boundary conditions used for FEA.

hip joint during walking was divided into 3 components, including a 200 N distal load along the femoral axis, a 40 N medial load, and a 50 N anterior load. The surface of the inferior end of the femoral model was completely confined to a site located at a distance of 20 mm from the distal end of the femoral stem (Fig. 1C).

Table 1 shows the YM and Poisson's ratio of each material [31,32]. In this study, the material property was presumed to be equivalent to that of Co–Cr–Mo alloy or Ti–6Al–4V alloy, which are used as clinical materials for the femoral stem, or that of the cortical bone. All materials were assumed to be homogeneous and linear elastic. The FEA was performed using a nonlinear analysis software (MSC Marc 2008, MSC Software, USA); the calculation was performed in an elastic region. The maximum principal stress vector of the superficial femoral stem stress occurring inside the groove was projected to the coronal plane of the femoral stem, as shown in Fig. 1B, and it was assessed quantitatively as the angle θ formed with the direction of the groove depth.

Animal experiments

The unipolar-type artificial hip joint stem with the oriented grooves on the proximal medial side was fabricated using the Ti–6Al–4V alloy that has widespread clinical use. The geometry of the stem was identical to that used in the FEA analysis. The grooves were introduced by machining using a 5-axis computerized numerically controlled turning center system (MAZAK INTEGREX 200-3; Yamazaki Mazak, Japan). Before implantation, the stem was autoclaved at 126 °C and 0.2 MPa for 10 min for sterilization. Four beagles aged approximately 2 years and weighing 13.8 ± 1.2 kg were used. Under anesthesia, the stem with ±60° and 0° grooves was implanted into the right femur, and the stem with ±30° and 0° grooves was implanted into the left femur. The beagles were individually caged (dimensions of cage: width, 74 cm; depth, 68 cm; and height, 63 cm).

After 24 weeks, the beagles were sacrificed and the implanted stems were removed with the femurs. Proper placement of the stems in the femoral marrow cavities was confirmed. There were no symptoms of loosening and sinking throughout the experimental period, and no inflammation was found around the implants. The bone specimens were immersed in a 10% formalin neutral buffered solution to avoid decay of the organic elements.

All animal studies were performed with the approval of the Institutional Animal Care and Use Committee of the Graduate School of Engineering, Osaka University (approval number 18-2-0).

Table 1
YM and Poisson's ratio of the materials used for FEA.

	Material	YM/GPa	Poisson's ratio
Implant (femoral stem)	Cortical bone	13	0.30
	Ti–6Al–4V alloy	110	0.34
	Co–Cr–Mo alloy	225	0.30
Femur	Cortical bone	13	0.30
	Trabecular bone	1	0.30

Analysis of bone quantity and bone quality inside the oriented groove

Bone specimens with the grooved stem were sectioned in a coronal plane at 100 μm thickness with a diamond band saw system (BS-300CP; Exakt Apparatebau, Germany) and stained with Haematoxylin and Eosin (HE). These specimens were observed with an optical microscope (Biozero BZ-8000, Keyence, Japan). The thin section was further observed under a polarized light microscope (BX60; Olympus, Tokyo, Japan) with polarizer and analyzer in cross position for assessing Col alignment in the grooves.

Sections 300-μm thick corresponding to a coronal plane were prepared from the proximal medial part of the stem using a diamond band saw system. Micro CT was operated at 25 kV and 100 μA to produce 3D images with a spatial resolution of 15.3 μm on each side for analyzing the newly formed bone mass in the grooves. The image was binarized and the bone volume fraction defined as bone volume/total volume of interest (total volume inside the groove) (BV/TV) was determined by TRI/3D-BON software (Ratoc System Engineering, Japan). The coefficient of variation (CV) was calculated by dividing the standard deviation (SD) by the mean value. A microbeam X-ray diffractometer (μXRD) with a transmission optical system (R-Axis BQ; Rigaku, Japan) was used to analyze the preferential BAp *c*-axis alignment. Mo–Kα radiation was generated at 50 kV and 90 mA. The incident beam was collimated into a 100-μm circular spot by a double-pinhole metal collimator and projected vertically onto the specimen to analyze the 2D distribution of the BAp *c*-axis alignment along the surface of the thin specimen. The diffracted beam was collected for 3600 s.

From the Debye ring obtained, the diffracted intensities (I) from (002) and (310) planes of BAp were integrated along the azimuthal angle (β) at angle steps of 1°. The (002) crystal plane is the representative plane of the BAp *c*-axis and the (310) plane is orthogonal to (002) plane. Intensity distributions as a function of β ($I(\beta)$) were approximated by the following elliptic polynomial function (subtracted by a constant c) using the least-square method [33]:

$$I(\beta) = \left\{ \frac{\cos^2(\beta-\mu)}{a^2} - \frac{\sin^2(\beta-\mu)}{b^2} \right\}^{\frac{1}{2}} - c \quad (1)$$

where a, b, c, and μ are the fitting parameters and μ is the angle at which the intensity peaks. Finally, the degree of the BAp *c*-axis alignment was calculated as the intensity ratio of (002)/(310) for each β, resulting in 2D BAp *c*-axis alignment along the plane vertical to the incident X-ray beam. The 2D distribution of BAp alignment was expressed as a radar diagram.

Statistical analysis

All data are presented as means ± SD. Two-tailed unpaired Student's *t*-test was performed, and $P<0.05$ was considered statistically significant. IBM SPSS Statistics Base 20 software for Windows (IBM, Japan) was used for the statistical analysis.

Results

Stress distribution in the oriented grooves estimated by FEA models

Fig. 2 shows the distribution of maximum principal stress on the groove at the proximal medial region of the femoral stem. Positive values show tensile stress, and negative values show compression stress. Compression stress was dominant in either of the groove angles, and the direction of the maximum principal stress vector tended to be different for each groove angle. The tendency was particularly strong in grooves that were oriented more toward the proximal side. In 60° grooves, a maximum principal stress distribution was found along the direction of the groove depth. The relative angle θ between the maximum principal stress direction and the direction of the groove depth, as well as its

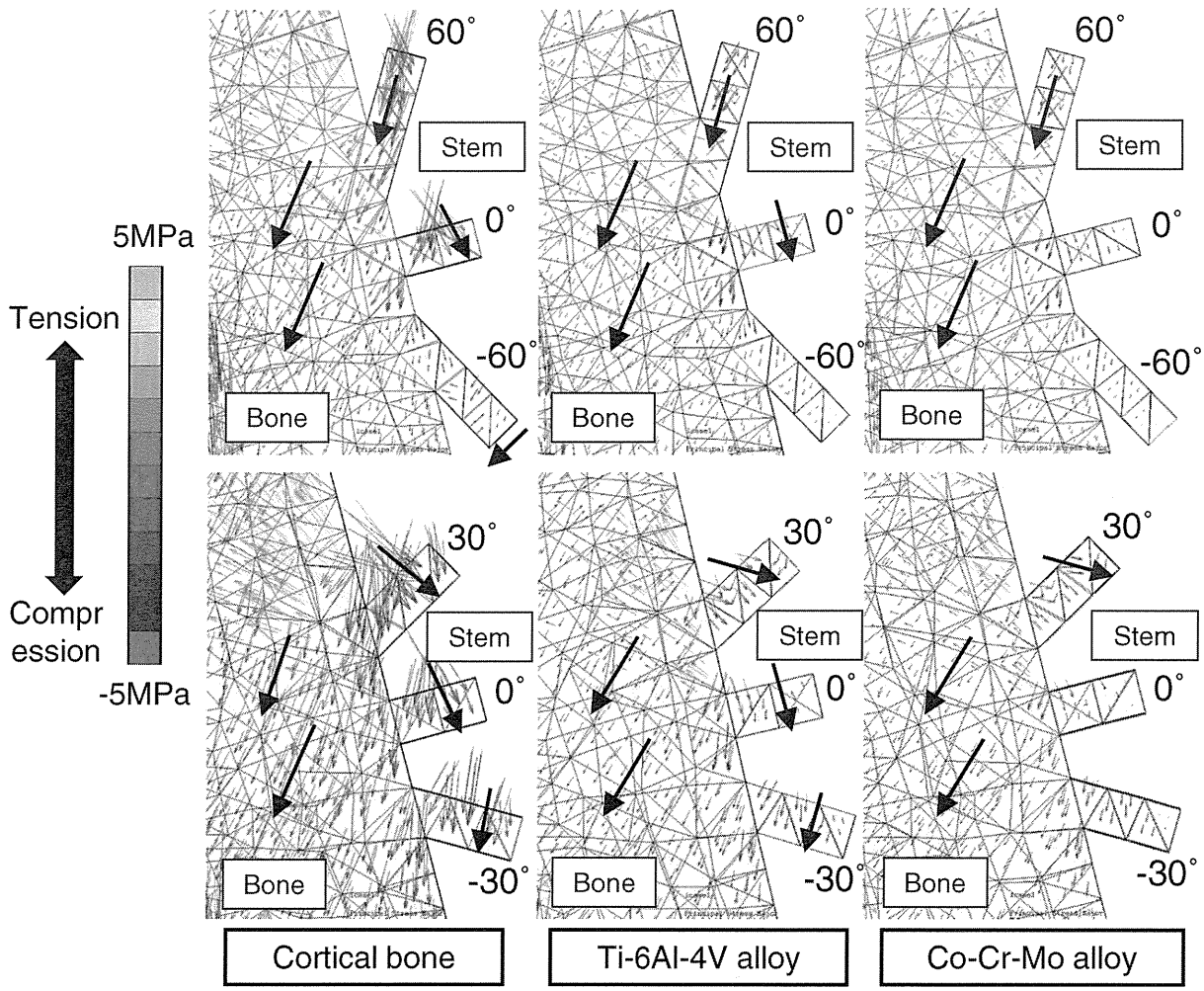

Fig. 2. Distributions of the maximum principal stress vectors in the groove and around the femoral stems made of cortical bone, Ti–6Al–4V alloy, and Co–Cr–Mo alloy.

absolute value, are plotted as in Fig. 3A. Each graph corresponds to the individual FEA element in the grooves. When the maximum principal stress direction followed the direction of the groove depth, the plot points in the figure were located near 0°. The maximum principal stress distribution inside the grooves varied depending on the groove angle and the material of the femoral stem. In particular, in the 60° grooves, the lower the YM of the femoral stem was, the higher the magnitude of the maximum principal stress and the better the consistency between the stress direction and the groove depth direction were observed. Meanwhile, in grooves with other angles, the maximum principal stress was barely parallel to the groove direction, and there was almost no continuity with the surrounding bone tissue. Around the root of the grooves, the principal stress tended to discontinuously distributed; the bone proximal to grooves was loaded in tension which would probably not occur if there were no grooves. The effect of this discontinuous distribution of the principal stress on bone ingrowth needed to be further investigated.

Fig. 3B shows the frequency of the maximum principal stress along the direction of the groove depth in each groove angle, and the YM of the femoral stem. The relative angle with the groove depth direction

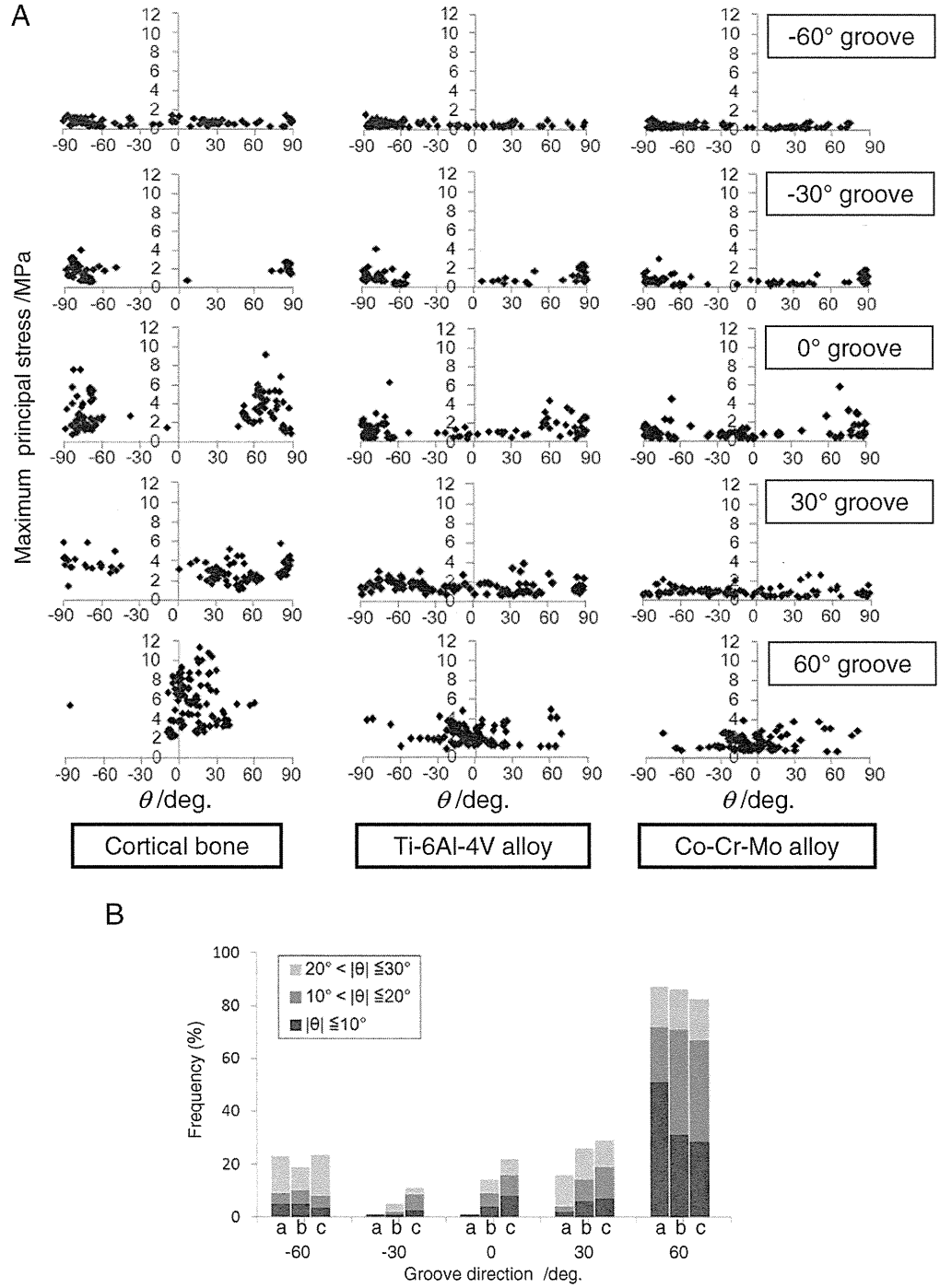

Fig. 3. Quantified distribution of the maximum principal stress in the grooves in terms of its magnitude and angle dependent on the groove angle and YM of the femoral stems. (A) Magnitude and relative angle (θ) between the direction of maximum principal stress and that of the groove depth. (B) Change in the frequency of the angle ($|\theta| \leq 30°$) between the direction of maximum principal stress and that of the groove depth. a: cortical bone, b: Ti–6Al–4V alloy, and c: Co–Cr–Mo alloy.